Computer Modeling in Engineering & Sciences

Tech Science Press

https://doi.org/10.32604/cmes.2026.086398

ARTICLE

Influence of Gas-Liquid Two-Phase Flow on Flow-Induced Vibration of Cylindrical Heat Exchange Tubes in Wind Turbine Heat Exchangers

Tianyu Song[1], Zeshuai Chen[2], Qian Chen[2], Ruiliang Wang[2,*], Congbo Zheng[1], Di Tang[1], Wenxi Shi[3] and Lang Xu[3]

[1]College of Mechanical Engineering, Zhejiang University of Technology, Hangzhou, China
[2]Windey Energy Technology Group Co., Ltd., Zhejiang Key Laboratory of Offshore Wind Power Technology, Hangzhou, China
[3]Hangzhou Turbine Power Group Co., Ltd., Hangzhou, China

*Corresponding Author: Ruiliang Wang. Email: wangrl@windeyenergy.com

Received: 29 May 2026; Accepted: 10 August 2026; Published: 21 October 2026

ABSTRACT: With the continuous increase in wind turbine capacity, the heat dissipation demands of key components such as converters and generators have become increasingly stringent. As a critical part of wind turbine thermal management systems, the reliability of heat exchangers is closely related to overall system stability. In this study, an efficient CFD–CSD coupling framework combined with a gas–liquid two-phase model was employed to establish a reduced-dimensional modeling approach for investigating the flow-induced vibration of cylindrical heat exchange tubes under cross-flow conditions. The proposed modeling strategy reduces computational complexity while retaining the dominant fluid–structure interaction characteristics, enabling efficient evaluation of vibration responses under different gas–liquid flow conditions. The coupled effects of gas–liquid phase evolution, hydrodynamic loading, flow structures, and structural response were analyzed. The results show that the tube exhibits periodic vibration in both drag and lift directions, while gas–liquid interaction leads to more complex flow structures and modifies the vibration behavior. With increasing void fraction, the drag-direction response decreases, whereas the lift-direction response shows a different variation trend. A transition from dispersed bubble structures to slug-like flow patterns was also observed with increasing gas content. The present study provides insight into the mechanism of gas–liquid two-phase flow-induced vibration and offers an efficient modeling approach for evaluation of heat exchanger vibration characteristics in wind turbine applications.

KEYWORDS: Gas-liquid two-phase flow; flow-induced vibration; CFD-CSD coupling; wind turbine heat exchanger; cylindrical heat exchange tube; structural stability

1 Introduction

With the rapid development of wind power technology, modern wind turbines are moving toward higher rated capacity, higher power density and more compact nacelle layouts. These trends increase the thermal load of generators, converters, gearboxes and control units, making heat dissipation a key factor affecting efficiency, reliability and service life [1]. For direct-drive wind turbines, the cooling system is essential for maintaining the generator and converter within safe thermal limits [2]. Recent studies on wind power converters have also shown that liquid cooling structures can effectively improve the heat dissipation performance of insulated-gate bipolar transistor modules [3]. In addition, thermal modeling of wind turbine generators indicates that external operating conditions can significantly affect the thermal state and cooling

Copyright © 2026 The Authors. Published by Tech Science Press. This work is licensed under a Creative Commons Attribution 4.0 International License, which permits unrestricted use, distribution, and reproduction in any medium, provided the original work is properly cited.

requirements of wind turbines [4]. Therefore, the heat exchanger, as a core component of the cooling loop, directly influences the stable operation of large-scale wind turbines.

When the cooling medium flows through or across heat exchange tubes, unsteady fluid forces are generated on the tube surface, which may cause flow-induced vibration. Flow-induced vibration of cylindrical structures has been systematically discussed in classical vibration theory [5]. For heat exchanger tube arrays, cross-flow-induced vibration is closely related to vortex shedding, turbulence-induced excitation and fluidelastic instability [6]. Fluidelastic instability is generally regarded as one of the most dangerous excitation mechanisms because the vibration amplitude may increase rapidly once the flow velocity exceeds a critical threshold [7,8]. For shell-and-tube heat exchangers, previous studies have established relatively complete analysis procedures involving flow excitation, damping, vibration response and fretting-wear assessment [9,10]. In practical heat exchangers, tube spacing, support stiffness, adjacent-tube motion and structural boundary conditions further change the dominant frequency and vibration amplitude. Recent coupling vibration analysis of heat exchanger tube bundles has confirmed that the interaction among neighboring tubes can significantly affect the vibration response of the target tube [11]. Hence, the vibration characteristics of cylindrical heat exchange tubes must be considered in the design of wind turbine heat exchangers.

Compared with single-phase flow, gas-liquid two-phase flow has more complex excitation characteristics. The interaction between bubbles, liquid phase and tube walls causes local fluctuations in void fraction, pressure and momentum, resulting in random and strongly nonlinear hydrodynamic loads. Experimental investigation on two-phase cross-flow-induced vibration of a confined cylinder has shown that void fraction and flow pattern strongly affect the vibration response [12]. For tube bundles, local-scale two-phase cross-flow experiments further indicate that bubble behavior and phase distribution can change the vibration characteristics of flexible tubes [13]. Equivalent load estimation in upward two-phase cross-flow also shows that hydrodynamic excitation in tube bundles is strongly affected by gas-liquid phase interaction [14]. Moreover, studies on the instability threshold of tube arrays in air-water cross-flow indicate that the coupled effects of liquid and gas phase Reynolds numbers should be considered when evaluating vibration risks [15]. These findings suggest that two-phase-flow-induced vibration remains a key uncertainty in the thermal-fluid-structural design of heat exchangers. Recent reviews have also pointed out that two-phase flow-induced vibration is affected by flow pattern, void fraction, mass flux, local geometry and structural boundary conditions [16].

Numerical simulation provides an effective method for analyzing the interaction between complex flow fields and structural vibration. For gas-liquid two-phase flow, the Volume of Fluid (VOF) method can capture the interface evolution between gas and liquid phases [17]. For structural vibration, simplified structural models such as the spring-mass-damping system are commonly adopted to describe tube responses under transient fluid excitation [18]. Coupled fluid-structure interaction (FSI) methods have been widely used to evaluate the deformation and vibration of elastic structures under unsteady flow conditions [19]. Recent studies have further extended these approaches to multiphase flow-induced vibration problems. Experimental investigations have demonstrated that two-phase flow regimes and phase distribution characteristics significantly affect the vibration response of cylindrical structures under cross-flow conditions [20]. Meanwhile, CFD-based fluid-structure coupling models have been successfully applied to heat exchanger tube bundles, revealing the influence of flow field characteristics and structural parameters on vibration behavior [11]. Compared with purely experimental approaches, coupled numerical simulations can provide detailed pressure, velocity, phase distribution and vibration response information, which is helpful for revealing the mechanism of two-phase-flow-induced vibration in wind turbine heat exchangers.

In this study, an established computational fluid dynamics–computational structural dynamics (CFD–CSD) coupling framework combined with a VOF multiphase model was employed to investigate the flow-induced vibration of cylindrical heat exchange tubes in wind turbine heat exchangers under gas–liquid two-phase cross-flow conditions. Unlike previous studies mainly focusing on single-phase flow-induced vibration or simplified fluid–structure interaction problems, this work extended the application of the coupling framework to multiphase flow environments relevant to wind turbine cooling systems. The effects of void fraction on vibration characteristics, hydrodynamic forces, and flow-field evolution were systematically investigated, with particular attention paid to the relationship between gas–liquid phase distribution, pressure variation, wake evolution, and directional vibration response. The results provide further understanding of the mechanisms governing gas–liquid two-phase flow-induced vibration and offer theoretical support for improving the structural reliability of compact heat exchanger systems in wind turbine applications.

2 Analysis Methods

At present, research on flow-induced vibration caused by gas-liquid two-phase flow mainly includes two aspects: experimental investigation and numerical simulation. Due to the inherent complexity of gas-liquid two-phase flow, experimental studies are usually difficult to conduct. For the external flow around cylindrical heat exchange tubes in wind turbine heat exchangers, the influencing variables become more complicated when the gas-liquid two-phase medium flows across the compact tube array. Meanwhile, the flow pattern becomes highly unstable, and the transient flow characteristics are difficult to predict accurately. In practical wind turbine heat exchangers, the compact arrangement of cylindrical tubes and the interaction between adjacent tubes further increase the complexity of the flow-induced vibration mechanism.

In this chapter, the CFD–CSD coupling framework combined with a gas–liquid two-phase flow model was extended to analyze the flow-induced vibration of cylindrical heat exchange tubes in wind turbine heat exchangers. A numerical model was developed and validated against experimental results, providing a reliable basis for investigating the vibration response mechanisms under gas–liquid two-phase flow conditions. The technical solution is illustrated in Fig. 1a.

2.1 Control Equations and Turbulence Model

For the two-dimensional incompressible viscous flow, the continuity equation is given by:

$$\frac{\partial u_i}{\partial x} + \frac{\partial v_i}{\partial y} = 0 \tag{1}$$

where i denotes the fluid phase, and u_i and v_i are the velocity components in the x and y directions, respectively.

The corresponding Navier–Stokes momentum equations are expressed as:

$$\begin{cases} \rho_i \left(\dfrac{\partial u_i}{\partial t} + u_i \dfrac{\partial u_i}{\partial x} + v_i \dfrac{\partial u_i}{\partial y} \right) = \mu_i \left(\dfrac{\partial^2 u_i}{\partial x^2} + \dfrac{\partial^2 u_i}{\partial y^2} \right) + \rho_i f_x - \dfrac{\partial p}{\partial x} \\ \rho_i \left(\dfrac{\partial v_i}{\partial t} + u_i \dfrac{\partial v_i}{\partial x} + v_i \dfrac{\partial v_i}{\partial y} \right) = \mu_i \left(\dfrac{\partial^2 v_i}{\partial x^2} + \dfrac{\partial^2 v_i}{\partial y^2} \right) + \rho_i f_y - \dfrac{\partial p}{\partial y} \end{cases} \tag{2}$$

In the equation, ρ_i represents the density of the fluid; f_x and f_y represent the external forces acting on a unit volume of the fluid; μ_i is the dynamic viscosity; and p_i is the pressure.

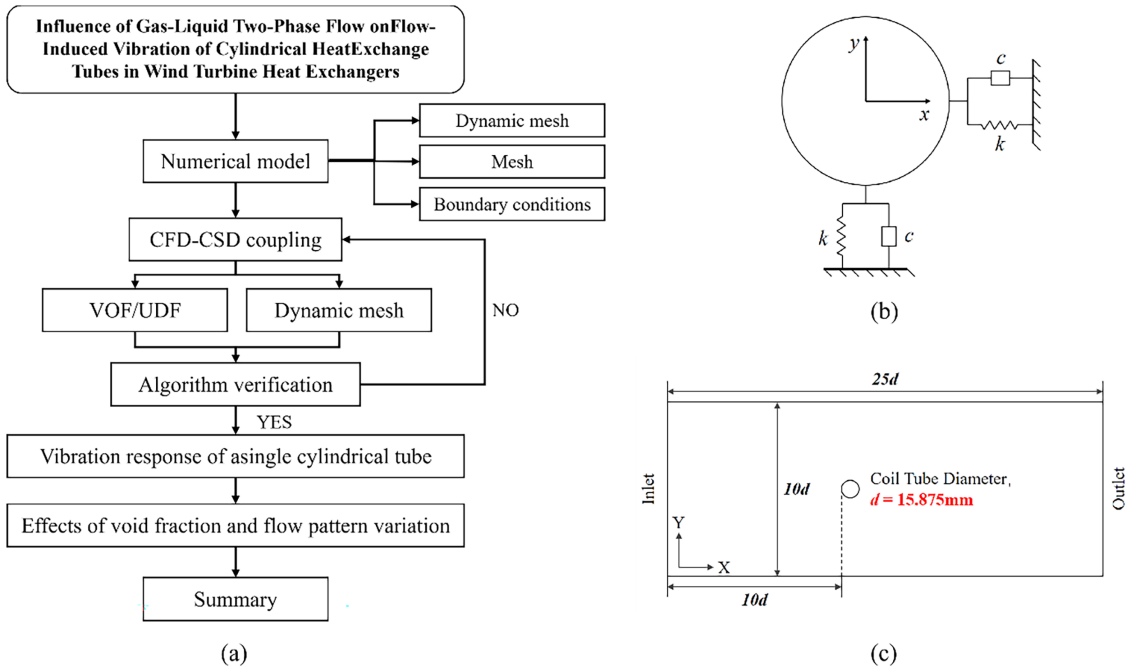


Figure 1: Numerical model and computational domain: (**a**) technical route; (**b**) two-degree-of-freedom vibration model; (**c**) tube-array computational domain.

Based on the evaluation by Tang et al. [21], the Transition shear stress transport (SST) model was selected due to its superior agreement with experimental data and its capability in resolving vortex shedding at the tube wake. The boundary conditions are summarized in Table 1. Pressure–velocity coupling was handled using the SIMPLEC algorithm, and spatial gradients were computed using the Least Squares Cell-Based method. The governing equations, including momentum, turbulent kinetic energy, specific dissipation rate, and intermittency, were discretized using a first-order upwind scheme, with pressure interpolation performed via the PRESTO! method. A convergence criterion of 10^{-6} was imposed for residuals. Default under-relaxation factors were adopted to ensure numerical stability. Transient simulations were conducted using a first-order implicit scheme.

Table 1: Boundary conditions for single tube model.

Project	Content
Solving Type	Pressure-based solver
Solving Method	Transient
Turbulence Model	Transition SST
Fluid Medium	Water/Air
Inlet Condition	Velocity inlet
Outlet Condition	Pressure outlet
Upper and Lower Boundaries	Symmetric boundary condition
Heat Exchange Tube Wall	No-slip wall
Two-phase Flow Model	VOF model

The Transition SST model was employed to resolve the near-wall transition, flow separation and wake evolution around the cylindrical tube. The transport equations for the transition momentum thickness Reynolds number $\widetilde{Re}_{\theta t}$ and intermittency factor γ are written as [22]:

$$\frac{\partial(\rho\tilde{R}e_{\theta t})}{\partial t}+\frac{\partial(\rho U_j\tilde{R}e_{\theta t})}{\partial x_j}=P_{\theta t}+\frac{\partial}{\partial x_j}[\sigma_{\theta t}(\mu+\mu_t)\frac{\partial\tilde{R}e_{\theta t}}{\partial x_j}] \tag{3}$$

$$\frac{\partial(\rho\gamma)}{\partial t}+\frac{\partial(\rho U_j\gamma)}{\partial x_j}=P_{\gamma1}+P_{\gamma2}-E_{\gamma1}-E_{\gamma2}+\frac{\partial}{\partial x_j}\left[\left(\mu+\frac{\mu_t}{\sigma_\gamma}\right)\frac{\partial\gamma}{\partial x_j}\right] \tag{4}$$

The transport equations for turbulent kinetic energy k and specific dissipation rate ω are:

$$\frac{\partial(\rho k)}{\partial t}+\frac{\partial(\rho k u_i)}{\partial x_i}=\frac{\partial}{\partial x_j}\left(\Gamma_k\frac{\partial k}{\partial x_j}\right)+G_k-Y_k \tag{5}$$

$$\frac{\partial(\rho\omega)}{\partial t}+\frac{\partial(\rho\omega u_j)}{\partial x_j}=\frac{\partial}{\partial x_j}\left(\Gamma_\omega\frac{\partial\omega}{\partial x_j}\right)+G_\omega-Y_\omega+D_\omega \tag{6}$$

In the equation, $P_{\gamma1}$ and $E_{\gamma1}$ represent the transition sources; $P_{\gamma2}$ and $E_{\gamma2}$ represent the sources of destruction and re-laminarization; σ_γ is a constant in the equation; $P_{\theta t}$ is the source term of the transport equation for $\tilde{R}e_{\theta t}$; G_k and G_ω are the production terms of turbulent kinetic energy and specific dissipation rate, respectively; Γ_k and Γ_ω are the effective diffusion coefficients; Y_k and Y_ω are the dissipation terms; and D_ω is the cross-diffusion term.

2.2 VOF Model

The gas–liquid two-phase flow was modeled using the Volume of Fluid (VOF) method, an Eulerian interface-capturing approach. Air and water were treated as immiscible phases sharing the same velocity and pressure fields, with the gas–liquid interface tracked by the local phase volume fraction. Under constant-temperature adiabatic conditions without phase change, interphase mass transfer and energy transport were neglected.

The volume fractions of the gas and liquid phases satisfy:

$$\alpha_g+\alpha_l=1 \tag{7}$$

where α_g and α_l denote the gas and liquid volume fractions, respectively. The transport equation for the gas volume fraction is expressed as

$$\frac{\partial\alpha_g}{\partial t}+\nabla\cdot\left(\alpha_g\mathbf{u}\right)=0 \tag{8}$$

where $\mathbf{u}$ is the shared velocity field. The liquid volume fraction is obtained as $\alpha_l=1-\alpha_g$. The local mixture density and dynamic viscosity are evaluated from the phase volume fractions:

$$\rho_m=\alpha_g\rho_g+\alpha_l\rho_l \tag{9}$$

$$\mu_m=\alpha_g\mu_g+\alpha_l\mu_l \tag{10}$$

where ρ_m and μ_m are the mixture density and dynamic viscosity, respectively, and the subscripts g and l represent the gas and liquid phases.

The void fraction α in this study was defined as the inlet volumetric gas fraction:

$$\alpha = \frac{Q_g}{Q_g + Q_l} \tag{11}$$

where Q_g and Q_l are the inlet volumetric flow rates of the gas and liquid phases, respectively. A uniform mixture velocity was imposed at the inlet, and the inlet gas and liquid volume fractions were specified according to the prescribed void fraction.

The gas–liquid interface was captured using an interface reconstruction scheme in the VOF formulation. Surface tension was treated using the continuum surface force (CSF) formulation:

$$\mathbf{F}_\sigma = \sigma \kappa \nabla \alpha_g \tag{12}$$

where σ is the surface tension coefficient and κ is the local interface curvature.

The computational domain was initialized using the same gas–liquid volume fraction as the corresponding inlet condition to maintain consistency between the initial phase field and the imposed inlet phase composition. The main VOF-related parameters and numerical settings are summarized in Table 2.

Table 2: VOF-related parameters and numerical settings.

Parameter	Setting/Value
Gas/liquid phase	Air/water
Phase change and mass transfer	Not considered
Phase properties	$\rho_g = 1.225$ kg·m^{-3}, $\mu_g = 1.789 \times 10^{-5}$ Pa·s; $\rho_l = 998.2$ kg·m^{-3}, $\mu_l = 1.003 \times 10^{-3}$ Pa·s
Interface scheme	Geometric reconstruction
Surface tension treatment	CSF model; $\sigma = 0.072$ N·m^{-1}
Wall contact angle	Not explicitly considered
Gravity	g = 9.81 m·s^{-2}, negative Y-direction
Single-tube cases	V = 0.1~0.6 m/s, $\alpha = 0.32$
Tube-array cases	V = 0.2 m/s, $\alpha = 0.04$~0.20
Reynolds number range	$Re \approx 1.57 \times 10^3$–$9.40 \times 10^3$
Time step/CFL	$\Delta t = 7 \times 10^{-5}$ s; CFL < 1.0

2.3 Structural Model

Because the deformation of the tube was negligible in practical applications, the influence of elastic deformation of the heat exchange tube was ignored in this study. Therefore, the tube was modeled as a rigid body. The vibration process was then simplified as a two-degree-of-freedom spring–mass–damper system, as shown in Fig. 1b. The vibration control equations are given as follows [23]:

$$\begin{cases} F_x(t) = m\dfrac{d^2x}{dt^2} + c\dfrac{dx}{dt} + kx \\ F_y(t) = m\dfrac{d^2y}{dt^2} + c\dfrac{dy}{dt} + ky \end{cases} \tag{13}$$

In the equation, $F_x(t), F_y(t)$ are the drag force and lift force, m is the mass per unit length, c is the damping coefficient, k is the stiffness, x, y are the vibration displacements of the heat exchange tube in the X and Y directions, respectively.

One circular cylinder was mounted as a spring-damper-mass system to study the fluid-elastic performances of the cylinder bundle according to the assumption in [23]. The cylinder can be free to vibrate in response to flow-induced forces in both the drag direction and the lift direction. The governing equations of motion with two Degree of Freedoms were obtained from Newton's second law of motion, which were described by [24]:

$$m_s\ddot{x} + c_s\dot{x} + k_s x = F_x(t, x, \dot{x}, y, \dot{y}) \tag{14}$$

$$m_s\ddot{y} + c_s\dot{y} + k_s y = F_y(t, x, \dot{x}, y, \dot{y}) \tag{15}$$

where m is the mass of the cylinder, c is the damping of the system, F is the fluid-induced force, x and y represent the vibration displacements of the tube in the drag and lift directions.

The equivalent structural parameters adopted in the two-degree-of-freedom model are summarized in Table 3. The natural frequency and damping ratio are obtained from the standard mass–spring–damper relationships:

$$f_n = \frac{1}{2\pi}\sqrt{\frac{k}{m}}; \zeta = \frac{c}{2\sqrt{km}} \tag{16}$$

where m, k, and c denote the equivalent mass, stiffness, and damping coefficient of the tube, respectively.

Table 3: Structural parameters.

Parameter	Symbol	Value
Equivalent mass per unit length	m	0.367 kg·m^{-1}
Equivalent stiffness per unit length	k	4.62×10^4 N/m^2
Equivalent damping coefficient per unit length	c	2.60 N·s/m^2
Equivalent natural frequency	f_n	56.5 Hz
Damping ratio	ζ	0.01

The lift coefficient and drag coefficient are defined as:

$$C_L = \frac{F_L}{0.5\rho d l V^2}; C_D = \frac{F_D}{0.5\rho d l V^2} \tag{17}$$

In the formula, F_L and F_D represent the lift and drag forces on the cylinder, respectively, and ρ is the density of the fluid; d is the diameter of the pipe; V is the inlet flow velocity; l is the axial length of the heat exchange tube and for the two-dimensional models, it is usually assigned the default value of 1 m.

In the reduced-order structural model, the support constraints of the heat exchange tube are represented by equivalent linear stiffness and damping in the drag and lift directions. This treatment allows the model to capture the dominant in-plane vibration response induced by cross-flow excitation, while avoiding the high computational cost of resolving the distributed flexibility of the full tube. Spanwise bending modes, tube-end constraints, contact between the tube and supports, and fretting-related nonlinearities are not explicitly resolved; therefore, the present structural model is used to evaluate the dominant force–displacement coupling and relative vibration trends rather than local structural stress or wear behavior.

2.4 CFD/CSD Coupling Algorithm for Gas-Liquid Two-Phase Flow

The CFD–CSD coupling framework adopted in this study is a well-established partitioned two-way fluid–structure interaction approach that has been developed and validated in our previous work [23]. In the present framework, the transient gas–liquid flow field is first solved using the CFD solver, and the instantaneous hydrodynamic forces acting on the heat exchange tube are transferred to the structural solver. The calculated structural displacement is subsequently returned to the fluid domain to update the tube boundary and mesh deformation, enabling time-accurate coupling between the flow field, structural response, and mesh motion. Compared with our previous study, which focused on the development and validation of the coupling methodology under simplified flow conditions, the present work extends its application to gas–liquid two-phase cross-flow in wind turbine heat exchanger systems. Therefore, the emphasis of this study is placed on revealing the physical mechanisms of two-phase flow-induced vibration rather than further developing the numerical coupling algorithm.

The coupling procedure within each physical time step is implemented as follows (Fig. 2):

(1) The transient two-phase flow field is solved, and the instantaneous drag and lift forces are obtained by integrating pressure and viscous stresses over the tube surface;
(2) The computed hydrodynamic forces are transferred to the structural solver as external excitation loads;
(3) The structural dynamic response is solved using a four-step Adams–Bashforth time integration scheme to obtain the tube displacement;
(4) The displacement is mapped back to the CFD domain, and the dynamic mesh is updated accordingly to accommodate the tube motion. Local mesh smoothing and re-meshing are applied when necessary to maintain mesh quality under large-amplitude oscillations.

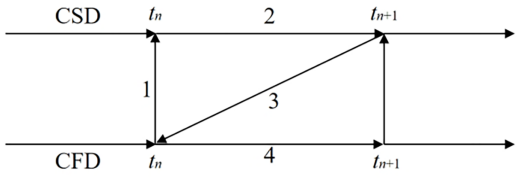


Figure 2: Schematic of CFD–CSD coupling procedure.

The heat exchange tube was treated as a rigid moving boundary, and the surrounding mesh was updated using a dynamic mesh technique. The outer boundaries remained fixed, while mesh deformation was mainly confined to the near-wall region to preserve boundary-layer resolution and numerical stability. Local smoothing and remeshing were applied when necessary to maintain mesh quality during large-amplitude oscillations. At each time step, the coupled system was iterated until the flow residuals decreased below 10^{-6}, with the transferred fluid forces and structural displacements reaching stable convergence. The time-step size was determined through temporal independence analysis and the characteristic vibration scale of the system to ensure adequate resolution of the dominant fluid–structure interaction response while maintaining computational efficiency.

2.5 Numerical Calculation Model

The numerical model represents the cross-flow region of compact tube-type heat exchangers in wind turbine thermal management systems rather than a specific commercial unit. A water–air two-phase flow was adopted as a representative working medium to account for gas entrainment, degassing, or incomplete venting in liquid cooling loops. The tube geometry, flow conditions, and equivalent support parameters

were defined to capture the dominant characteristics of two-phase-flow-induced vibration. Therefore, the model should be regarded as a physics-based representation for investigating vibration mechanisms rather than a direct reproduction of an industrial heat exchanger. To reduce computational cost while preserving the dominant flow-induced vibration characteristics, a two-dimensional model was employed. Since the present study focuses on cross-flow-induced vibration in the plane normal to the tube axis, the drag- and lift-direction responses can be effectively captured. Previous studies have shown that two-dimensional models accurately predict the dominant vibration amplitudes and frequencies of circular-cylinder cross-flow, although three-dimensional effects may influence local flow structures and instantaneous responses [25]. Therefore, despite neglecting spanwise variations, tube-end effects, and complex three-dimensional gas–liquid structures, the present model is sufficient to capture the dominant wake evolution, hydrodynamic excitation, and relative vibration trends under different void fractions.

The outer diameter of the heat exchange tube, d, is 15.875 mm, and the overall size of the computational domain is $10d \times 25d$. The cylindrical heat exchange tube is positioned at a distance of $10d$ from the inlet to ensure that the incoming flow has sufficient development space before reaching the tube. The single-tube configuration is shown in Fig. 1c.

The grid quality is critical to the reliability of numerical simulations. Considering the regular arrangement of the heat exchange tubes, a structured grid was adopted in this study. The structured mesh provides improved orthogonality and controlled grid distribution around the tube surfaces, enabling accurate resolution of near-wall flow characteristics while maintaining computational efficiency for transient CFD-CSD coupling. The grid model is shown in Fig. 3. Due to the large velocity gradient of the fluid around the pipe wall, a more detailed grid was needed to accurately capture the flow field changes. Therefore, the boundary layer mesh with a geometric growth rate was set near the pipe wall in this paper to ensure the calculation accuracy of the flow field near the pipe wall. To ensure the dimensionless wall distance $y^+ < 1$ in the calculation, the height of the first layer grid at the wall was 8×10^{-3} mm, the mesh growth rate was set to 1.1, with a total of 20 layers. And set this part of the grid as a rigid body, the red part in the picture. The grid area within a certain range near the heat exchange tube was set as a dynamic region to ensure that the grid could shrink or expand to fit the new boundary region when the heat exchange tube was displaced instantaneously, as shown in the orange region.

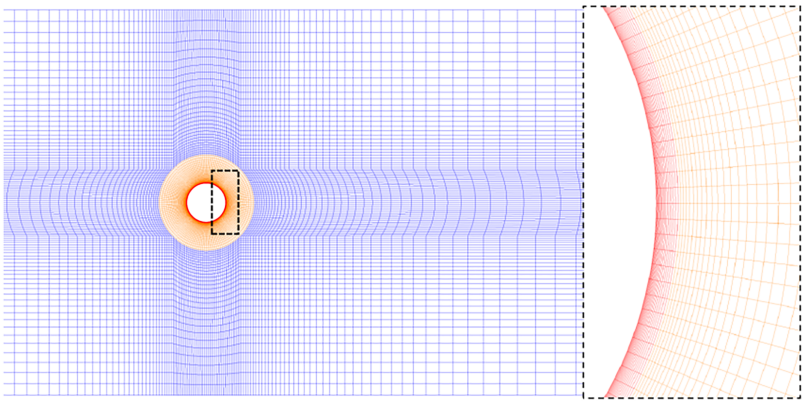
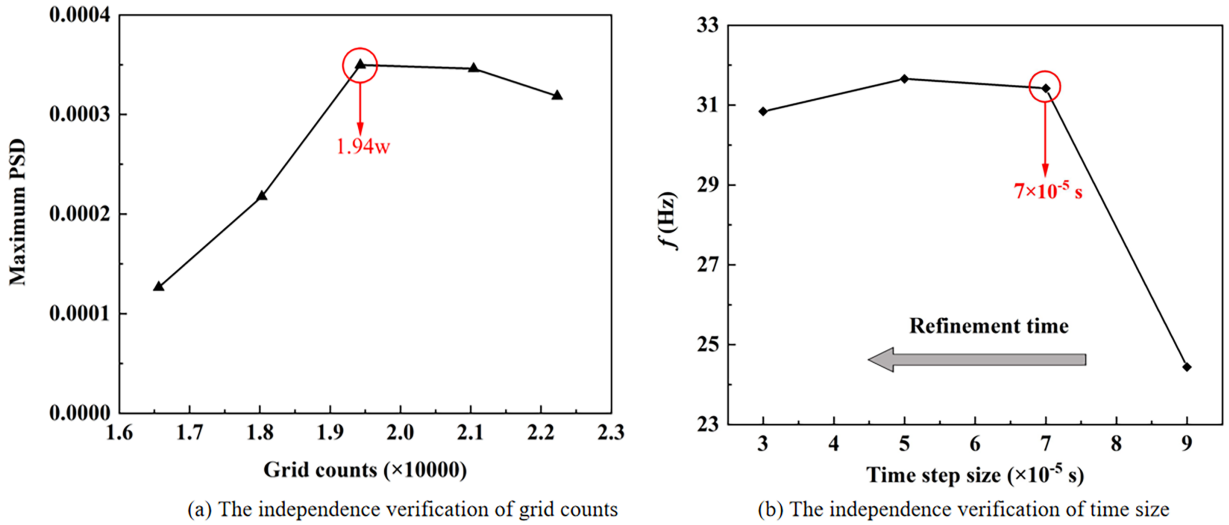


Figure 3: Structured mesh of the tube-array model.

Independence verification is an important step in the process of grid division, mainly to ensure that the grid model and time step are independent of the simulation results. Systematic grid convergence analysis and temporal resolution verification were implemented as demonstrated as shown in Fig. 4. The baseline grid

counts that satisfied the fundamental boundary layer resolution criterion ($y^+ < 1$) were established firstly, successive coarsening and localized refinements were systematically implemented to evaluate sensitivity across critical flow regimes. A total of five different grid models were established, with the number of grids being 16,600, 18,000, 19,400, 20,900, and 22,300. The uniform velocity water flow was used as the boundary condition of the inlet, and the lift coefficient of the target heat exchange tube surface was monitored. Then, the time domain signal of the lift coefficient was converted into a frequency domain signal by fast Fourier transform (FFT), and its maximum Power Spectral Density (PSD) was extracted, which is an important parameter to describe the power distribution of the signal response in the frequency domain. The peak value of power spectral density corresponds to the power of the amplitude at a specific frequency. The higher the power spectral density is, the larger the amplitude of the lift coefficient is. The maximum power spectral density of the heat exchange tube was calculated to verify the influence of the number of grids on the simulation results, as shown in Fig. 4. The increase in maximum PSD from 16,600 to 19,400 cells is attributed to the improved resolution of near-wall flow and wake fluctuations, as the relatively coarse mesh may underestimate the hydrodynamic response. Further refinement beyond 19,400 cells leads to negligible PSD variation, indicating that the dominant flow characteristics are adequately resolved. Therefore, the 19,400-cell mesh was adopted in the present study.



(a) The independence verification of grid counts (b) The independence verification of time size

Figure 4: The independence verification of grid counts and time step size.

In numerical simulation, the time step is the discretization interval of the simulation time, which defines how often the solver updates the solution during the simulation. Generally speaking, the smaller the time step, the higher the accuracy of the simulation results, especially when dealing with rapidly changing flow fields, but too small a time step will often increase a lot of calculation time. However, too large a time step will reduce the accuracy of the simulation results, but in some cases, adjusting the time step properly can help speed up the convergence of the calculation. Therefore, the choice of time step is very important for the accuracy and efficiency of numerical simulation results. The time step was rigorously determined through a CFL condition guided initial estimation followed by systematic scaling analysis, thereafter, four different time steps of 3×10^{-5} s, 5×10^{-5} s, 7×10^{-5} s, and 9×10^{-5} s were tested respectively using the verified grid model. Since the time step had a great influence on the frequency accuracy of the dynamic response of the heat exchange tube, this paper verified the influence of the time step on the simulation results by extracting the frequency corresponding to the amplitude of the maximum lift coefficient. As the time step was 9×10^{-5} s, the frequency corresponding to the amplitude of the maximum lift coefficient of the heat exchange

tube was only 24.444 Hz; when the time step was reduced to less than 7×10^{-5} s, its frequency was stable around 31 Hz. With the decrease of the time step length, the calculation results remained basically unchanged. Therefore, the maximum time step while ensuring the accuracy of the calculation was selected, the time step taken in all calculation conditions in this paper was 7×10^{-5} s taking into account both calculation accuracy and efficiency.

2.6 CFD/CSD Coupling Calculation Method Verification

To ensure a reasonable and reliable numerical simulation, it is of great significance to verify the accuracy of the CFD/CSD coupling solution method used in the current research. Therefore, a numerical calculation model was mainly established based on the flow around a single cylinder test conducted by Khalak and Williamson [26], and the accuracy of the CFD/CSD coupling method and two-dimensional model adopted in this paper was verified. The natural frequency of the cylinder was set to 0.62625 Hz following the methodology described in the reference. Bidirectional coupling between the cylinder motion and hydrodynamic forces was achieved by using the aforementioned User-Defined Function (UDF) and dynamic mesh settings. Based on the single-tube configuration, the transient solver method discussed in Section 2.2 was employed to calculate the cylinder's vibration response across varying flow velocities.

A comparison of the maximum dimensionless amplitude (Y/D) at different reduced velocities (U/f_nD) between the experimental measurements and numerical results is presented in Fig. 5. The experimental data are shown as scatter points, while spline-interpolated curves are used only to illustrate the overall response trends. The relative errors at selected points, represented by gray bars, were calculated based on the fitted curves. The numerical results show good agreement with the experimental measurements, accurately reproducing the increasing trend of vibration amplitude with increasing reduced velocity and capturing the characteristic vortex-induced vibration (VIV) response near the critical reduced velocity of approximately 2.5. The maximum relative deviation between the numerical and experimental results was approximately 15%, which is mainly attributed to differences between the numerical model and experimental conditions, including structural simplifications and experimental uncertainties. This deviation is considered acceptable because the simulation successfully reproduces the main vibration trends and characteristics observed experimentally, demonstrating the reliability of the CFD–CSD coupling framework and the two-dimensional tube model for investigating flow-induced vibration responses.

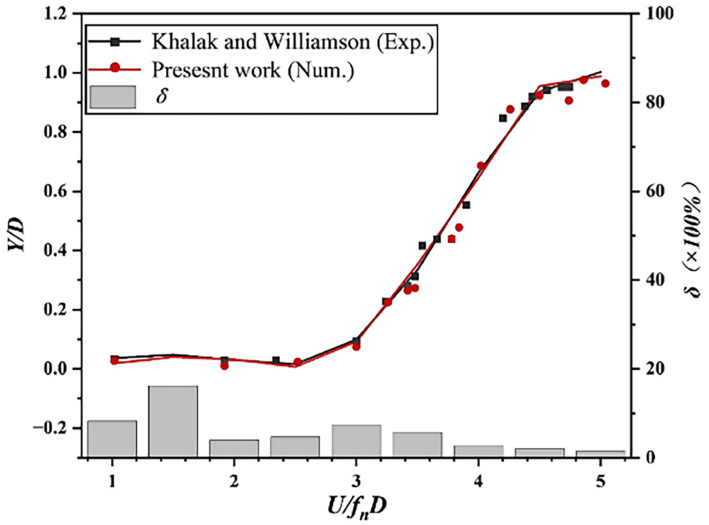


Figure 5: Comparison of dimensionless vibration amplitude (Y/D) under different reduced velocities (U/f_nD).

The above benchmark primarily validates the CFD–CSD coupling response under reference conditions. Additional support for the two-phase framework is provided by previous experimental and validated numerical studies. Experimental investigations have demonstrated the sensitivity of cylinder and tube-bundle vibrations to gas–liquid cross-flow conditions [12,13]. Meanwhile, VOF-based simulations of two-phase heat exchangers have shown reliable predictions of flow patterns and interface evolution, with deviations generally within acceptable ranges [27,28]. These studies support the phase-dependent excitation and gas–liquid interface mechanisms considered in this work. Therefore, the present validation is mainly intended to verify the reliability of the CFD–CSD coupling framework rather than provide a complete quantitative validation of all two-phase tube-array phenomena.

3 Vibration Response of the Heat Exchange Tube

Compared with single-phase flow, multiphase media exhibit more complex flow characteristics due to interfacial interactions and phase distribution variations, making their transient behavior more difficult to predict. Additionally, the presence of gas–liquid interfaces introduces additional complexity and instability into the flow patterns compared with single-phase flow conditions [29]. The heat exchange tube will be affected by the gaseous and liquid components at the same time. The vortex shedding, transverse force, and coupled vibrating are the prerequisites that the two-phase flow influences the tube. Therefore, research on the vibration of one single tube was conducted to verify these phenomena. Detailly, six different flow rates were selected, and water and air were used as the flow medium to observe the change of displacement response, velocity response, and lift force of the heat exchange tube under different flow speeds. The void fraction was set to 0.32 in the gas-liquid two-phase condition and the single-phase flow condition for comparison.

3.1 Displacement Time Domain Signal

The time-domain displacement responses of the tube subjected to single-phase and gas–liquid two-phase cross-flows at various inlet velocities V are presented in Fig. 6, where V denotes the uniform inflow velocity prescribed at the computational domain inlet. Under single-phase conditions, the response undergoes a brief initial transient before converging to steady periodic oscillations, characterized by well-defined waveforms and nearly invariant peak amplitude with no evident attenuation or stochastic fluctuations in the steady regime. In contrast, two-phase flow exhibits distinct temporal behavior: an initial transient with elevated X-direction amplitude decays progressively until a statistically stationary state is reached; unsteady gas–liquid interfaces and local void fraction perturbations introduce stronger temporal irregularity and amplitude fluctuations relative to the single-phase case. Quantitatively, the X-direction vibration amplitude under two-phase flow is consistently larger across all tested velocities, and the overall vibration intensity increases monotonically with inflow velocity for both regimes; as V rises from 0.1 to 0.6 m/s, the peak X-direction displacement and corresponding RMS amplitude under two-phase flow increase from 0.0462 to 0.2788 mm and from 0.0065 to 0.0570 mm, respectively, vs. 0.0010–0.0476 and 0.0009–0.0378 mm for single-phase flow. These findings corroborate that gas–liquid two-phase flow substantially amplifies vibration unsteadiness, which may exacerbate flow-induced fatigue risk in heat exchanger tubes under prolonged service.

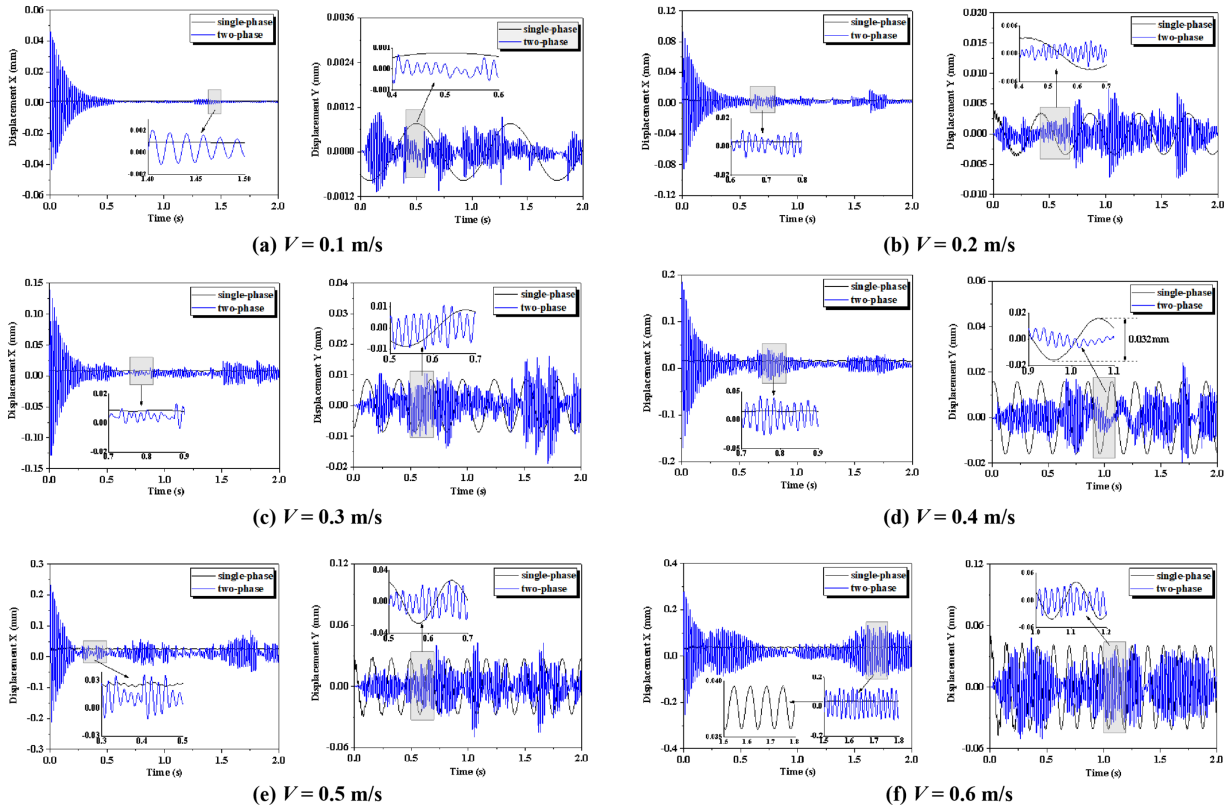


Figure 6: Time-domain vibration displacement responses of a single heat exchange tube.

The root mean square (RMS) amplitude in the X and Y direction were compared as shown in Fig. 7. In the X direction, the RMS amplitude under two-phase flow conditions is generally higher than that under single-phase conditions. At inlet velocities below 0.5 m/s, the RMS amplitudes of the two cases exhibit similar trends, although the gas–liquid two-phase flow produces a higher vibration response. As the inlet velocity increases to 0.6 m/s, the difference between the two cases becomes more significant, indicating an enhanced influence of gas–liquid interaction on tube vibration. This phenomenon is attributed to intensified gas–liquid interactions and wake disturbance at higher flow velocities, which enlarge the gap in hydrodynamic loading between single-phase and two-phase flows. In the Y direction, the vibration displacement of the heat exchange tube fluctuates around the equilibrium position at Y = 0 mm. The dominant vibration frequency of the tube rises with increasing flow velocity, while the Y-direction vibration amplitudes of the two cases are largely comparable. As the flow velocity increases from 0.1 to 0.6 m/s, the Y-direction vibration amplitude of the two-phase case increases from 0.0011 to 0.0482 mm, with the corresponding RMS amplitude rising from 0.0003 to 0.0186 mm. For the single-phase case, the vibration amplitude increases from 0.0008 to 0.0496 mm, and the corresponding RMS amplitude rises from 0.0005 to 0.0291 mm. Overall, two-phase flow enhances the X-direction RMS amplitude but reduces the Y-direction RMS amplitude. This divergent trend between drag-direction (X) and lift-direction (Y) responses stems from their distinct excitation mechanisms. The drag force is dominated by momentum transfer from the continuous liquid phase, and gas–liquid interfaces further augment flow unsteadiness and drag loading. In contrast, the lift response is governed by periodic vortex shedding. The presence of gas phases disrupts the coherent wake structures and weakens vortex shedding intensity, resulting in a lower lift-induced vibration amplitude under two-phase flow conditions.

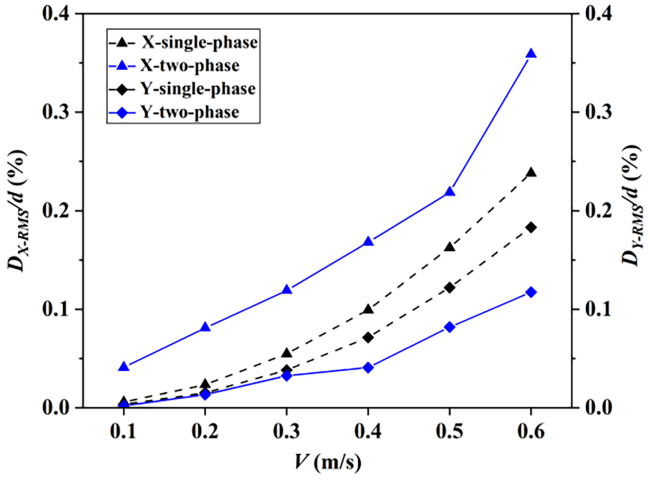


Figure 7: Comparison of RMS amplitudes in X and Y direction.

3.2 Velocity Time Domain Signal

The velocity response of the structure is a critical issue in the fluid-induced vibration of the heat exchange tube. The influence of fluid flow on the vibration can be understood by monitoring the velocity response of the heat exchange tube. Vibration is due to the fluid-structure interaction where flow produces active forces on the structure surface, causing the tube to vibrate. On the other hand, tube vibration also changes the generated active forces interactively. For the gas-liquid two-phase flow, the velocity response is also affected by the gas-liquid two-phase distributions and flow patterns. In this section, the velocity response of a single heat exchange tube with different flow rates was monitored and analyzed.

The vibration speed of the heat exchange tube increases with the flow rate, as shown in Fig. 8. In the X direction, the velocity response is consistent with the displacement response of the two-phase case. A large vibration amplitude is found at the initial stage, the amplitude was gradually weakened and converged to a constant range as time went by. When the flow rate increased from 0.1 to 0.6 m/s, the RMS velocity of the heat exchange tube in the X direction increased from 2.311 to 19.34 mm/s of the two-phase case, while the one increased from 0.0006 to 0.4892 mm/s of the single-phase case. In the Y direction, the velocity RMS of the heat exchange tube increased from 0.1075 to 6.4836 mm/s of the gas-liquid two-phase case, while the one increased from 0.0041 to 1.4083 mm/s of the single-phase case. The velocity response was enhanced by the gas–liquid two-phase flow in both the X and Y directions, which differs from the displacement response. Under low flow velocity conditions, the velocity response of the single-phase case remains almost the same, without obvious vibration period and amplitude change. When the flow velocity increased to 0.5 m/s, the velocity response gradually began to show a dominant period and amplitude, as shown in Fig. 8b. It is also estimated that liquid with a larger density increased the tube vibration in the drag direction while a smaller amount of gas decreased the tube vibration in the lift direction.

3.3 Frequency Characteristics of the Heat Exchange Tube

To further analyze the vibration frequency under the gas-liquid two-phase flow, the vibration displacements of the heat exchange tube under different flow velocities were transformed into the frequency domain using the Fourier transform. At present, the vibrating mechanism of heat exchange tubes in single-phase flow have been investigated to find the periodic, stable, and corresponding flow patterns. However, the vibration amplitude of the heat exchange tube in the X direction is often larger than that in the Y direction under the

erosion of gas-liquid two-phase flow. Therefore, the vibration amplitude and frequency in the X direction cannot be ignored for the gas-liquid two-phase case, and the frequency domain displacement response with different flow rates are further compared as shown in Fig. 9.

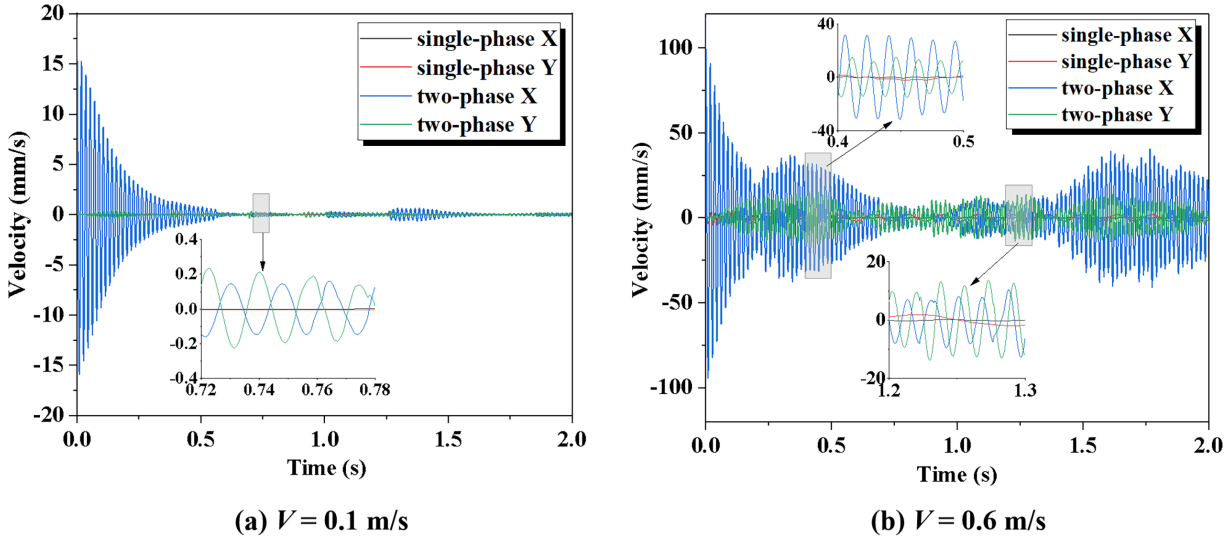


Figure 8: Time-domain vibration velocity response of single heat exchange tube.

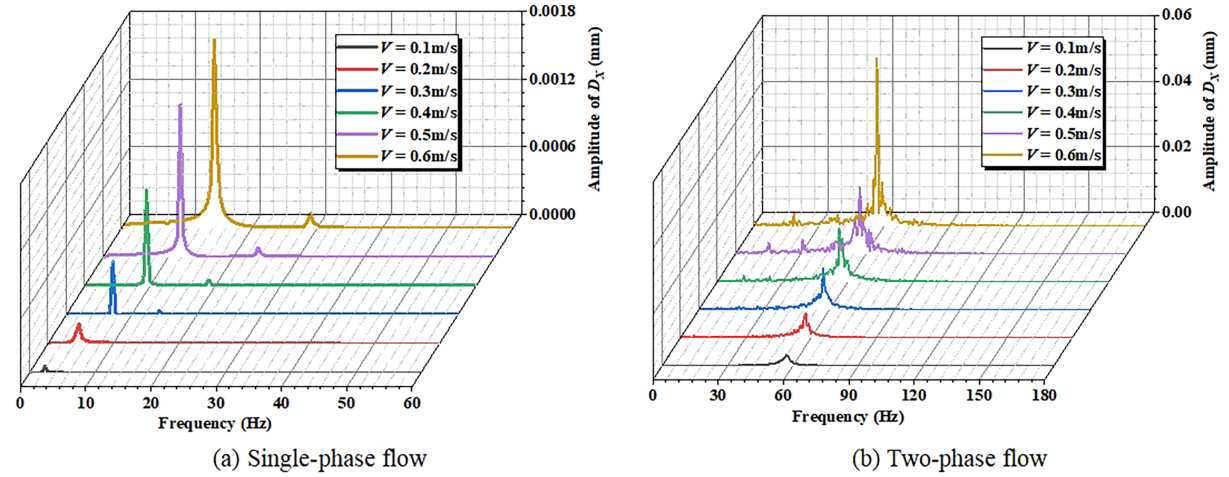


Figure 9: Frequency domain response of vibration displacement in the X direction.

The investigation of dominant vibration frequencies holds critical significance, revealing not only resonance risks when matching structural natural frequencies which substantially accelerates fatigue, but also serving as a diagnostic marker for distinguishing failure mechanisms. Its multifaceted implications extend to operational health monitoring and standards-compliant vibration mitigation design. The frequency and amplitudes associated with the dominant frequency were compared for both single-phase and gas-liquid two-phase conditions, as shown in Fig. 10. An obvious peak value in the low-frequency region is observed in the single-phase flow condition in the X direction, which was regarded as the dominant frequency. The dominant frequency was only 2.38 Hz when the gas flowed at 0.1 m/s, and it increased with the flow velocity.

Another secondary frequency was observed which was larger than the dominant frequency. In contrast, the dominant frequency of the two-phase flow is mainly concentrated within 56~58 Hz, which was much higher than the one in the single-phase flow conditions. It is interesting to find a clear linear correlation between the vibration frequency and the flow rate for the single-phase condition. Conversely, the vibration frequency appears to be independent of the flow rate for the two-phase condition and confined to a narrow range. The amplitude increased steadily with the flow rate until reaching 0.5 m/s and then rapidly increased for the two-phase case. Notably, the amplitude in the gas-liquid two-phase case was substantially greater than in the single-phase case at the same flow rate.

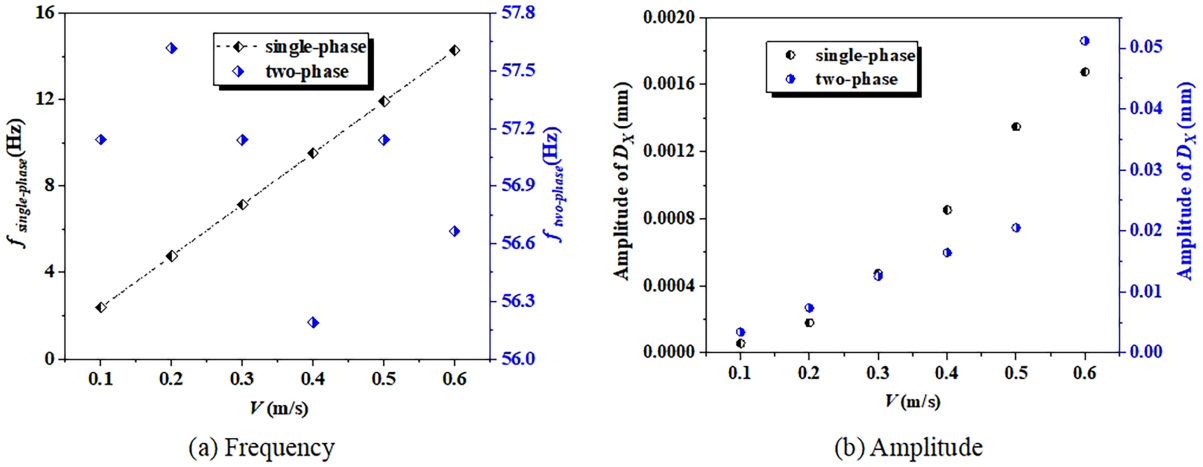


Figure 10: Comparison of dominant frequency and amplitude in X direction.

In the Y direction, the vibration exhibited similarities to the X direction for the gas-liquid two-phase case, the amplitude escalated as the flow rate. The dominant frequency was predominantly confined within the range of 55 to 59 Hz, which is broader than the single-phase case. The dominant frequency showed no obvious dependence on flow velocity, whereas the vibration amplitude generally increased with increasing flow velocity, unlike the single-phase case. Interestingly. The amplitude of the single-phase case was larger than that of gas-liquid two-phase flow which is contrary to the X direction. Furthermore, the comparative analysis of the dominant frequency in different directions of single-phase flow indicated that the dominant frequency of the X direction is approximately twice the Y direction for each flow rate then brought the characteristic "8" shaped vibration trajectory. The analysis elucidated that the heat exchange tube primarily produced vibrations in the y-direction with a relatively narrow frequency range of single-phase case. In contrast, under the gas-liquid two-phase case, a broader frequency spectrum and a higher dominant frequency were exhibited with smaller amplitudes. The lift force was mainly associated with vortex shedding-induced pressure fluctuations, while the drag force was dominated by momentum transfer from the continuous liquid phase.

4 Investigation of the Two-Phase Flow on Tube Array Vibrations

Compared with single-phase flow, the hydrodynamic interactions of gas-liquid two-phase flow are more complex, which may produce bubbles, liquid film, slippage, and other phenomena, which lead to uneven fluid distribution on the shell side, making the fluid force on the surface of the tube more difficult to predict. There are relatively many characteristic parameters to characterize the flow field, the void fraction (α) is an important parameter because it is necessary to determine density, pressure, and other variables [30],

which could change the flow rule and pattern of gas-liquid two-phase flow [31], resulting in various vibration amplitudes of the heat exchange tube. This chapter carried out the calculation under different void fractions, comprehensively analyzed the influence on the fluid-induced vibration of the tube array from the perspective of the time domain and frequency domain, and observed the flow field distribution and flow characteristics.

4.1 Tube-Array Numerical Calculation Model

Wind turbine heat exchangers usually contain compactly arranged cylindrical heat exchange tubes to meet the cooling requirements of high-power components. In practical operation, the cooling medium flows across the tube bundle, and the interaction between the unsteady flow field and the tube structure may induce vibration of the heat exchange tubes. To analyze the flow-induced vibration characteristics under gas-liquid two-phase flow conditions, the complex heat exchanger structure was simplified into a two-dimensional cylindrical tube array model, as shown in Fig. 11. The middle tube in the tube array was selected as the target monitoring tube, denoted as T1. In the tube array model, the diameter of the cylindrical heat exchange tube, d, is set as 15.875 mm. The transverse tube spacing, l, and the longitudinal tube pitch, h, are set as 23.622 and 23.707 mm, respectively. To reduce the influence of the upper and lower wall boundaries on the internal flow structure, the tubes located at the upper and lower boundaries are simplified as half tubes, and symmetric boundary conditions are applied. The computational model contains 31 circular tubes and 8 half tubes with symmetric boundaries. To better capture the flow structure and wake evolution around the tube bundle, a refined mesh region with a length of $5d$ was arranged downstream of the tube array. In addition, inlet and outlet extension sections with a length of $20d$ are set before and after the tube array, respectively, to ensure sufficient flow development at the inlet and reduce the influence of the outlet boundary on the internal flow field.

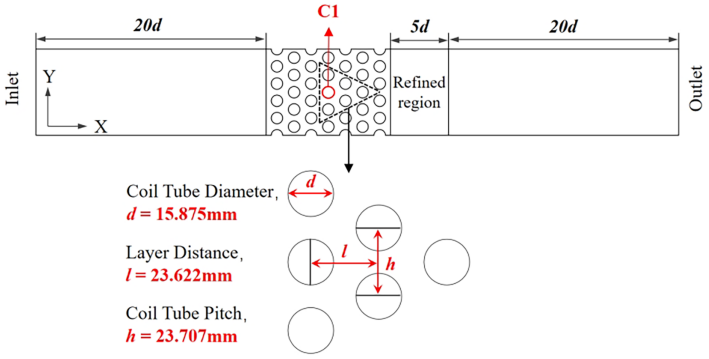


Figure 11: Two-dimensional tube-array model of the heat exchanger.

The height of the first layer grid at the wall was set as 8×10^{-3} mm according to the y^+ criterion, the mesh growth rate was set to 1.1. The red-colored grid region was designated as rigid-body domains, as illustrated in Fig. 12. The grid area within a certain range near the heat exchange tube was set as a dynamic region to ensure that the grid could shrink or expand to fit the new boundary region when the heat exchange tube vibrated instantaneously, as shown in the orange region.

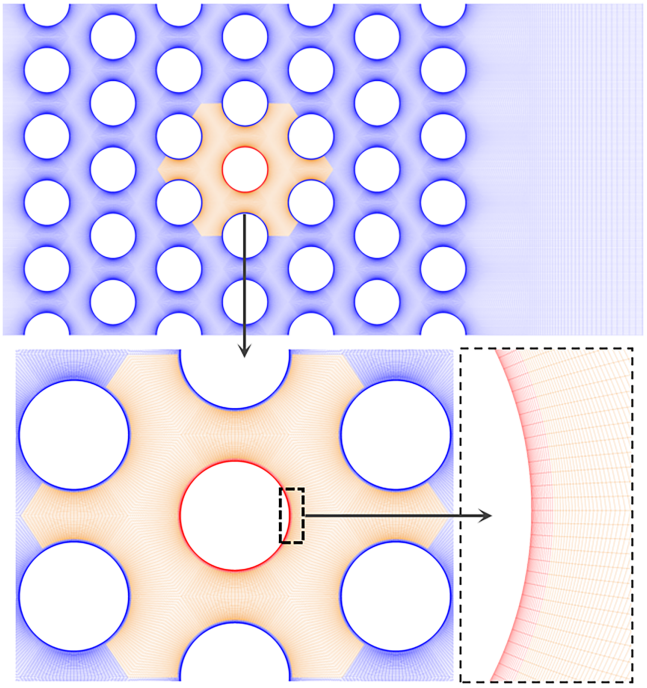


Figure 12: Rigid-body and dynamic-mesh regions of the tube-array model.

In this paper, six grid models with different cells (296,800, 364,800, 434,100, 502,200, 569,000, 637,000) were established to analysis the grid number independence. The uniform flow was used as the boundary condition of the inlet, and the lift coefficient of the target heat exchange tube was monitored. The calculation of the maximum power spectral density (PSD) to verify the independence of grid number, as shown in Fig. 13a. When the grid number reaches 502,200, the number has an insignificant impact on the maximum power spectral density. Finally, the 502,200 cells model was adopted for flow-induced vibration study of gas-liquid two-phase flow considering numerical accuracy and efficiency. On the other hand, time step independence verification is also crucial for numerical simulation. Four different time steps (3×10^{-5}, 5×10^{-5}, 7×10^{-5}, 9×10^{-5}) were set to study the independence verification of time step size using the verified grid model. Similarly, the Fourier transform (FFT) was used to obtain the frequency response of the calculated lift coefficient, as shown in Fig. 13b. It is shown that the time step has a great influence on the frequency accuracy. The dominant frequency is 24.4 Hz when a time step with 9×10^{-5} s was used. When the time step was reduced below 7×10^{-5} s, the dominant frequency converged to a stable value of 31 Hz. Therefore, 7×10^{-5} s was adopted as the time step in the current investigation.

4.2 Dynamic Responses of the Tube

Under different void fractions, the flow law and flow pattern are very different, the fluid force generated becomes more complex, and the vibration amplitude of the heat exchange tube is also different, as shown in Fig. 14. The dominant frequencies of vibration range from 53 to 56 Hz. In the X direction, the peak frequency response amplitude decreases with increasing void fraction. When the void fraction is 0.08, the peak response amplitude decreases by only 1.6%, while the reduction becomes more evident with further increases in void fraction. The tube vibration is mainly dominated by the X direction, whereas the Y-direction vibration amplitude is smaller. In the Y direction, the peak response amplitude shows no clear variation trend with void fraction. When the void fraction increases from 0.04 to 0.16, the peak response amplitude fluctuates

significantly, and it decreases when the void fraction reaches 0.16. In the low-frequency region, a secondary dominant frequency was found with 15 Hz only in the *Y* direction. The secondary vibration amplitude was slightly higher than the *X* direction, and the secondary vibration amplitude gradually decreased with the increase of the void fraction.

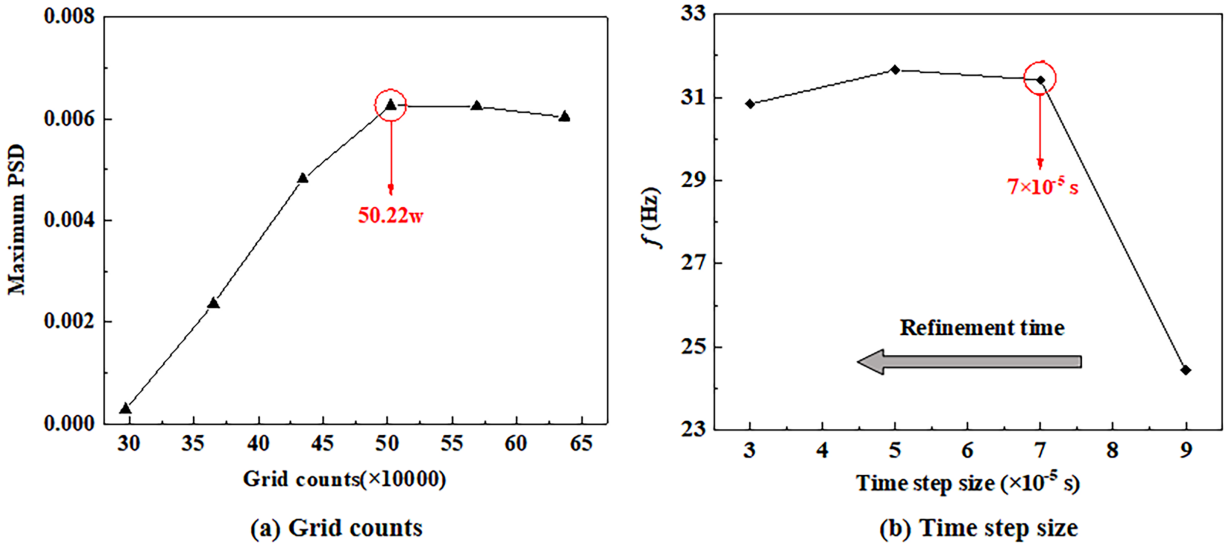


Figure 13: Grid independence verification: (**a**) the influence of the number of grids on the maximum power spectral density; (**b**) the influence of time step on frequency accuracy.

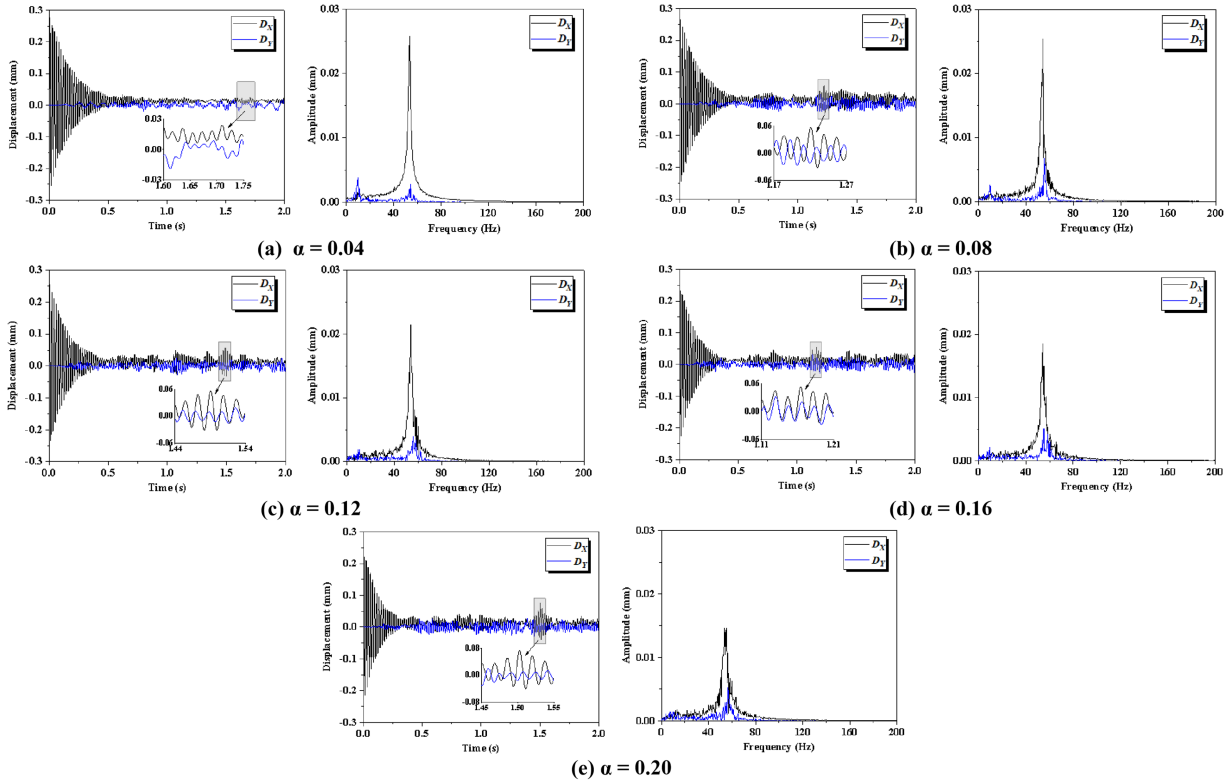


Figure 14: Vibration displacement of target tube T1.

The peak response and root-mean-square (RMS) amplitudes were further calculated for the tube array model. The vibration of the heat exchange tube is dominated by the X-direction component. In terms of frequency response, the vibration amplitudes of tube T1 in the X direction are consistently larger than those in the Y direction under all working conditions. The maximum X-direction vibration amplitude decreases with increasing void fraction. As shown in Fig. 15a, the amplitude D_x decreases from 0.026 to 0.014, and its descent rate becomes approximately constant when the void fraction exceeds 0.08. Fig. 15b presents the RMS amplitudes of target tube T1 in both the X and Y directions. The X-direction RMS amplitude decreases with rising void fraction, whereas the Y-direction RMS amplitude shows an increasing trend. The X-direction vibration amplitude remains larger than its Y-direction counterpart across all cases. This directional dependence of vibration amplitudes arises from the distinct fluid dynamic behaviors in gas–liquid two-phase flows. The underlying physical mechanism is further elaborated in Section 4.3 through analysis of pressure redistribution and gas–liquid flow evolution around the tube. As the X-direction response dominates the overall vibration characteristics, it is the critical component for fluid-induced vibration assessment and merits focused investigation.

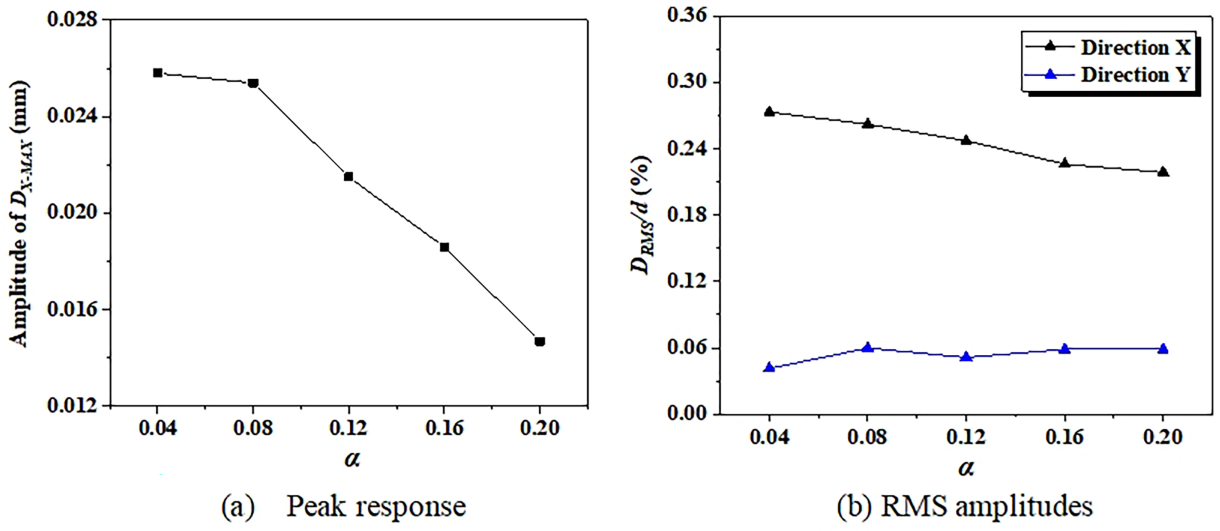


Figure 15: Vibration response characteristics of target tube T1 under different void fractions: (**a**) peak displacement in the X direction; (**b**) RMS amplitudes.

The lift/drag coefficient of the target tube T1 was monitored to obtain the time domain response. Then, the Fast Fourier Transform was used to convert the time domain responses into the frequency domain responses, as shown in Fig. 16. When the void fraction is 0.04, the maximum amplitude of the drag coefficient achieves 0.0358, and the lift coefficient achieves 0.02. When the void fraction is 0.08, the maximum amplitude of the drag coefficient achieves 0.0326, and the lift coefficient achieves 0.0149. Compared to the case with 0.04 void fraction, the maximum amplitudes of the drag coefficient and lift coefficient have been decreased by 8.9% and 25.5%, respectively. When the void fraction is 0.16, the maximum amplitude of the drag coefficient achieves 0.0262, and the lift coefficient achieves 0.0128. When the void fraction is 0.2, the maximum amplitude of the drag coefficient achieves 0.0223, and the lift coefficient achieves 0.0096. Compared to the void fraction of 0.16, the maximum amplitudes of the drag coefficient and lift coefficient have been decreased by 14.9% and 25%, respectively. As a result, there was no obvious change in the time domain response, as shown in Fig. 16a. In addition, the maximum drag coefficient decreased gradually with increasing void fraction. The peak lift coefficient showed an overall decreasing trend, except for an increase from 0.0116 at α = 0.12 to 0.0128 at α = 0.16, corresponding to a 10.3% increase. This local rebound may result from the

different responses of drag and lift forces to gas-liquid flow evolution, where the flow pattern transition around α = 0.16 temporarily alters wake instability and enhances lift fluctuations.

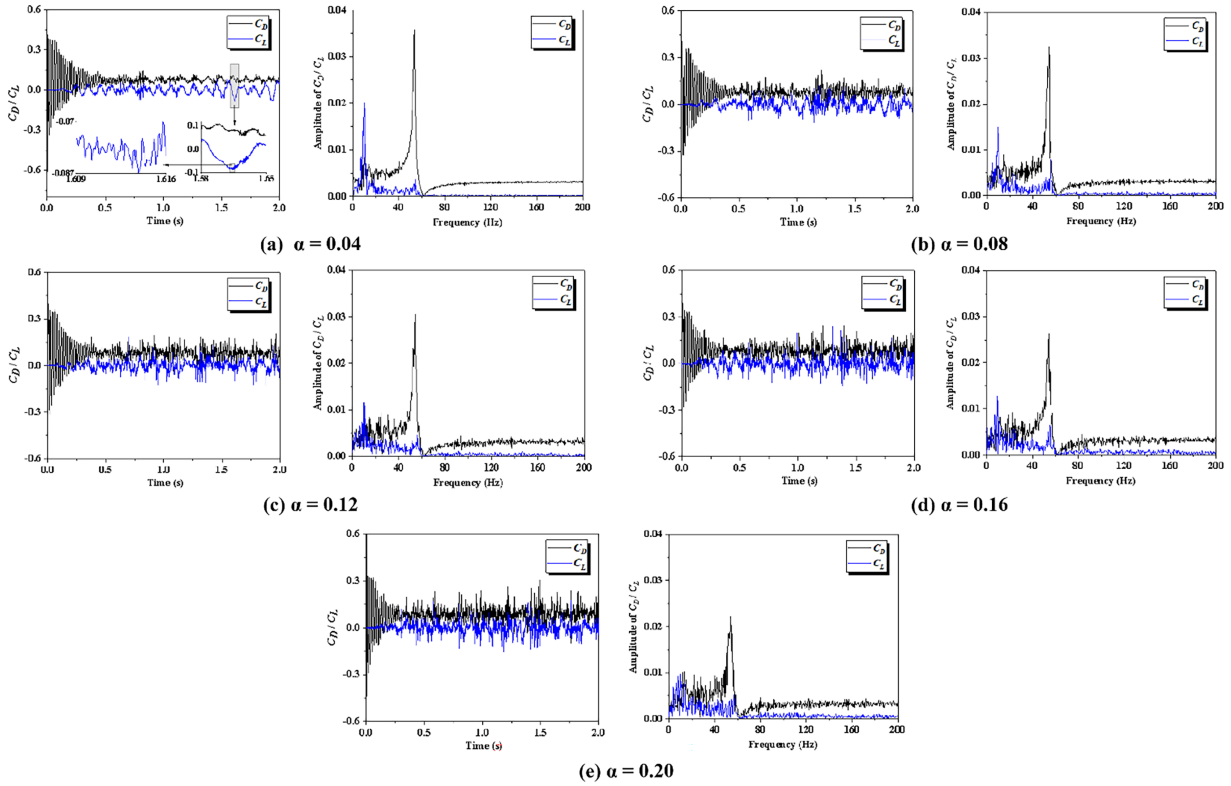


Figure 16: Lift and drag coefficient of target tube T1.

4.3 Flow Patterns in the Gas-Liquid Two-Phase Flow

The representative pressure contour of the flow field is shown in Fig. 17. It can be observed that the pressure field exhibits a continuous decay along the flow direction, while the pressure asymmetry around the tube generates directional hydrodynamic loading. The pressure of the flow field remains similar under different void fractions. For the same column of heat exchanger tubes, the pressure near the inlet was higher than the outlet, and a 600 Pa pressure drop was found for the 7 rows of tubes. By contrast, there was no large differential pressure in the Y direction.

The pressure distribution provides a direct link between the gas-liquid flow field and the vibration response. The asymmetric pressure loading between the upstream and downstream sides of the tube generates the dominant hydrodynamic excitation in the drag direction, which explains the larger X-direction vibration response observed in Fig. 14. Meanwhile, the evolution of the gas-liquid interface modifies the local pressure fluctuation and wake structure, resulting in changes in the unsteady fluid loading acting on the tube.

To analyze the pressure exerted on the target heat exchanger tube T1, the surface pressure coefficient was used to characterize the pressure distribution around the tube. The pressure coefficient was calculated using the following equation:

$$C_P = \frac{P_\theta - P_0}{\frac{1}{2}\rho V_P^2} \tag{18}$$

where θ is the angle between the flow velocity direction and the surface of the heat exchange tube illustrated in Fig. 18, P_θ is the surface static pressure, P_0 is the inflow static pressure, V_P is the inflow velocity.

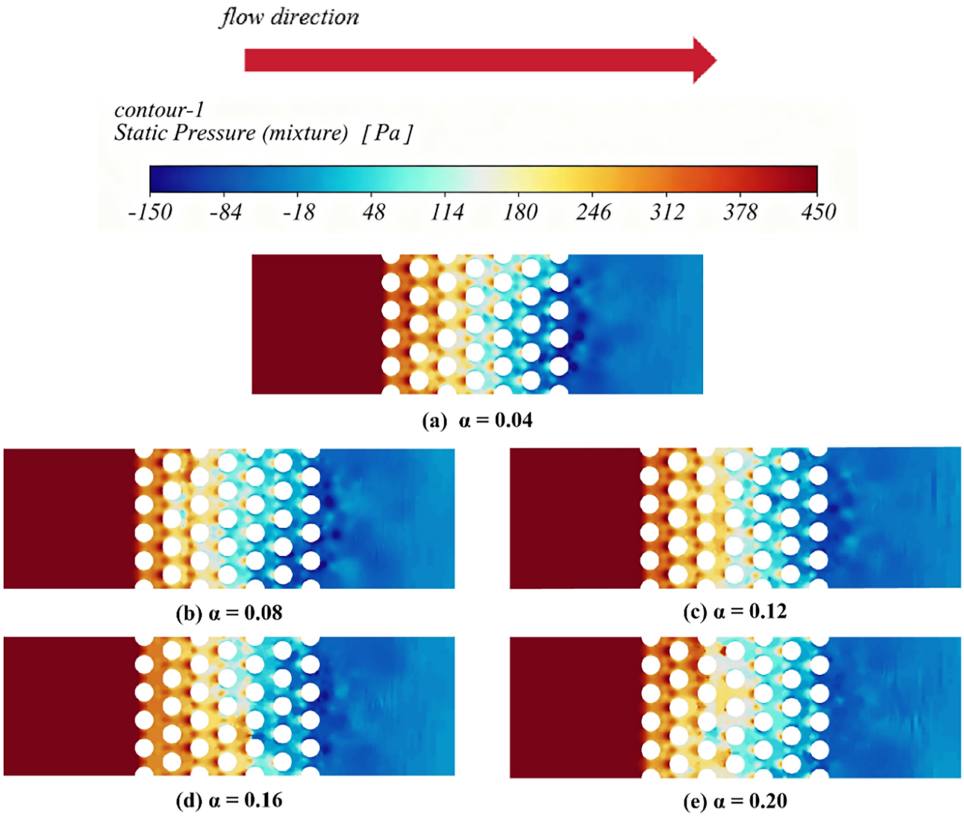


Figure 17: Pressure distributions of the flow field under different void fractions.

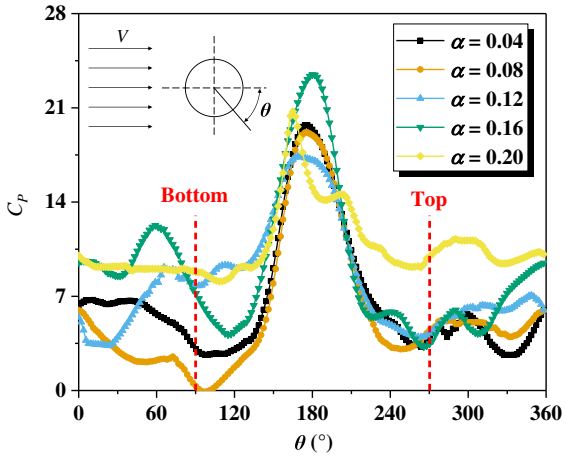


Figure 18: Surface pressure coefficient of target tube T1 under different void fractions.

The surface pressure coefficient of the target tube T1 was extracted in different void fractions, as shown in Fig. 18. As can be seen, the maximum pressure coefficient appeared at $\theta = 180°$, which corresponds to the central position on the inlet side of the heat exchange tube. The pressure coefficients on the bottom and top

surface were generally less at θ = 90° and θ = 270°. At the same time, the pressure coefficients on the top and bottom surfaces had a relatively small differential pressure, whereas a significant pressure difference was observed between the upstream (θ = 180°) and downstream (θ = 0°/360°) sides.

The typical velocity distribution of the flow field in different void fractions was illustrated in Fig. 19, it can be observed that the velocity of the gas-liquid mixture fluctuated in the range of 0~0.9 m/s. However, due to the decrease in the tube pitch, the velocity will be increased. When the gas-liquid mixture flowed around the heat exchanger tube, it created a high flow velocity region on the top and bottom surface, which was the maximum velocity in the flow field.

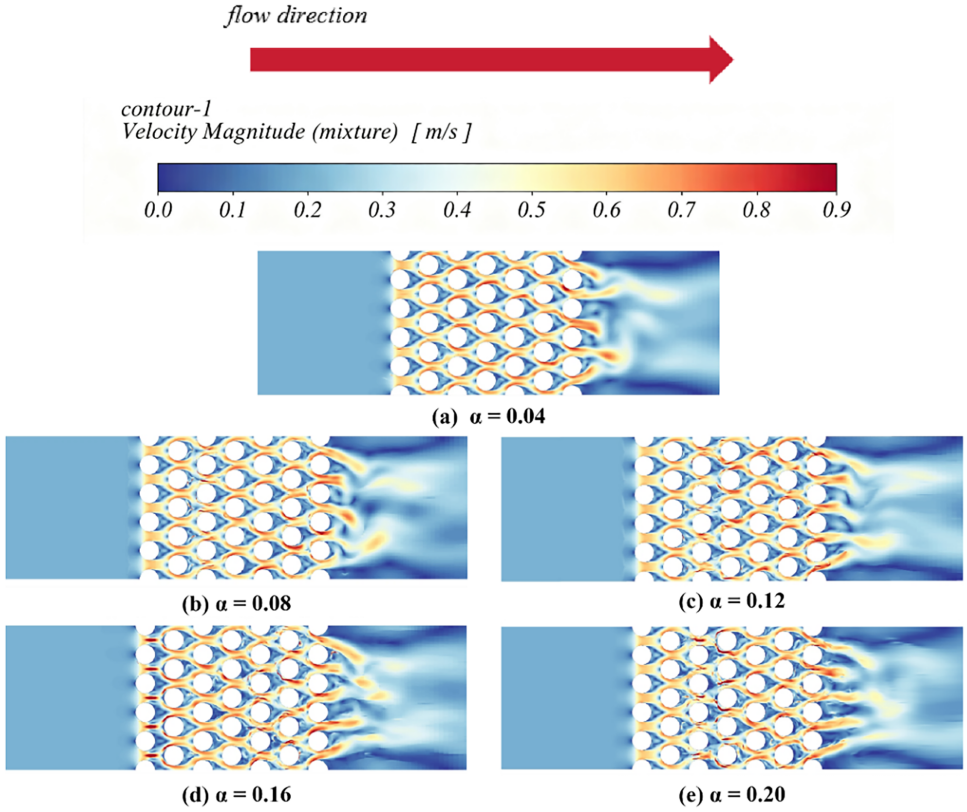


Figure 19: Velocity distributions of the flow field under different void fractions.

As shown in Fig. 20, the formation and disappearance of high flow velocity (v > 0.6 m/s) within a period T. At 1/8 T, both the lower surface of A1 and the upper surface of A4 had a high flow velocity. As the calculation time progresses, the high flow velocity area on the lower surface of A1 became smaller, while the high flow velocity area on the upper surface of A4 became larger. At 4/8 T, the high flow velocity area on the lower surface of A1 disappeared, while the high flow velocity area on the upper surface of A4 continued to increase. In the whole process, there was no direct transfer between the two high-flow velocity areas, the formation and disappearance appeared to be occurring synchronously. At 1/8 T, the upper surface of A3 had an obvious high flow velocity area. At the same time, there was a persistent high flow velocity area on the lower surface of A5. And from 1/8 to 4/8 T, there was a clear trend of increasing velocity. Therefore, it can be inferred that the fluid within the high-velocity region on the upper surface of A3 was mainly transported to the lower surface of A5, while the formation of the high-velocity region on the upper surface of A4 was mainly associated with

fluid transported from the lower surface of A1. During the transfer process, the flow velocity did not remain the characteristic of high flow velocity.

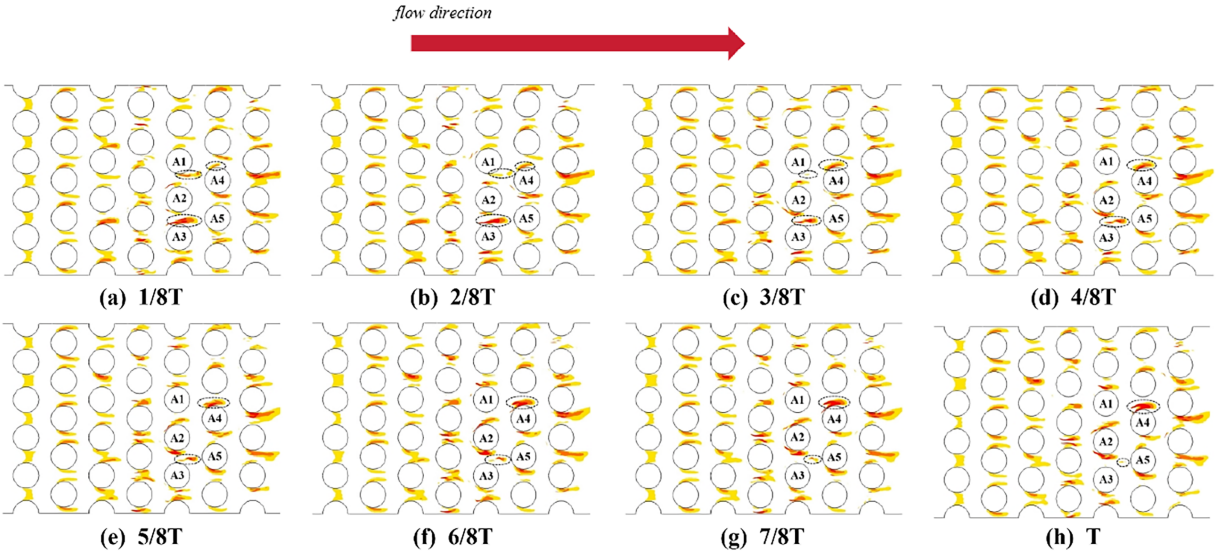


Figure 20: Evolution of high-velocity regions around the tube array.

The gas–liquid two-phase flow pattern has a significant influence on the flow characteristics around the cylindrical tube. To investigate the effect of void fraction on the flow regime, a series of simulations with void fractions ranging from 0.04 to 0.20 was performed, as shown in Fig. 21. In the present study, the flow regimes were qualitatively identified based on the morphology of the simulated gas–liquid interface in conjunction with the corresponding void fraction. Therefore, the identified flow patterns represent the evolution observed in the present numerical simulations rather than rigorous flow regime boundaries. As the void fraction increases, the proportion of the gas phase (white region) gradually increases, resulting in increasingly complex gas–liquid flow structures. When the void fraction is lower than 0.08, the flow is characterized by dispersed bubble structures, with discrete gas bubbles uniformly distributed throughout the liquid phase, as shown in Fig. 21a–e. As the void fraction increases, enhanced bubble interaction, coalescence, and interfacial deformation promote the formation of elongated gas structures. At α = 0.12, slug-like flow characteristics begin to appear, where elongated gas pockets intermittently separated by liquid regions can be observed. This observation is based on the evolution of gas-phase morphology and interfacial characteristics in the present simulations and should not be interpreted as a universal transition threshold. With a further increase in void fraction, the elongated gas structures become more pronounced, indicating a progressive evolution toward a slug-flow-dominated pattern. At α = 0.20, periodic vortex shedding is observed, accompanied by periodic low-pressure regions in the wake. This phenomenon contributes to the decrease in the time-averaged pressure coefficient on the rear side of the tube, as shown in Fig. 18.

Nine critical frames in a vibration period were extracted to study the dynamic change of the gas-liquid two-phase flow to obtain the flow rule of the bubbles, as shown in Fig. 22. At t_n, the relatively large bubbles (Q1) occurred in the lower right corner of A1, as shown in Fig. 22a. At t_{n+2}, the bubbles (Q1) were divided into two parts. One part did not separate from the heat exchanger tube but adhered to the tube wall, and the other part flowed downstream, which was the dominant part of the bubbles (Q1). At t_{n+7}, the bubbles began to separate into the bubbles (Q2) and the bubbles (Q3). The dominant bubbles flowed downstream to come up with some new shedding bubbles, those bubbles paired up with each other to pass downstream as

a pair of corotating bubbles till the flow outlet. The dominant bubbles and other auxiliary bubbles paired up with each other to form a jet flow between neighboring tubes due to the staggered arrangement, as shown in Fig. 22d–i. However, there were no two identical bubbles in the whole flow domain, which implied that statistics and randomness were the two main characteristics of the bubble shedding.

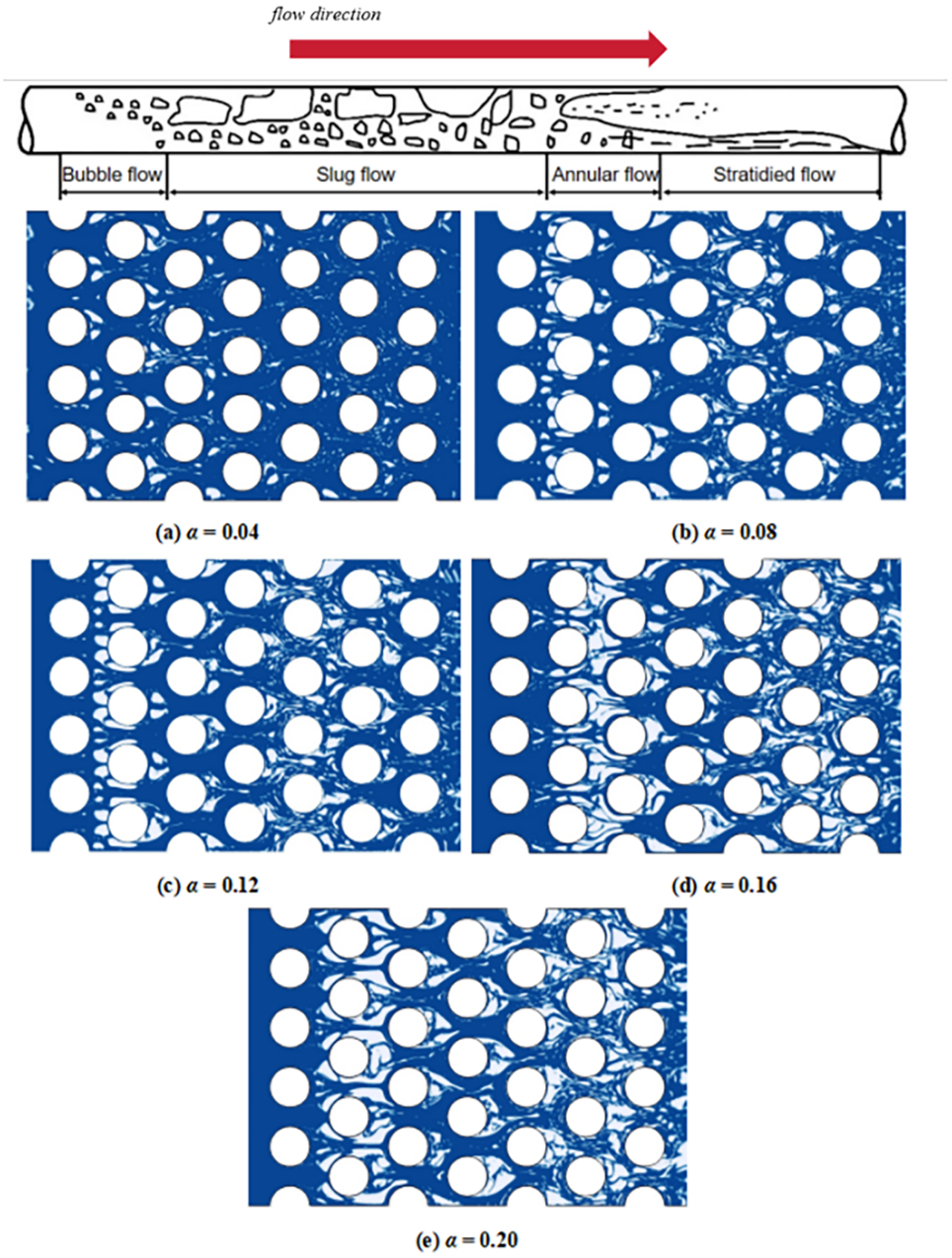


Figure 21: Gas–liquid flow patterns under different void fractions.

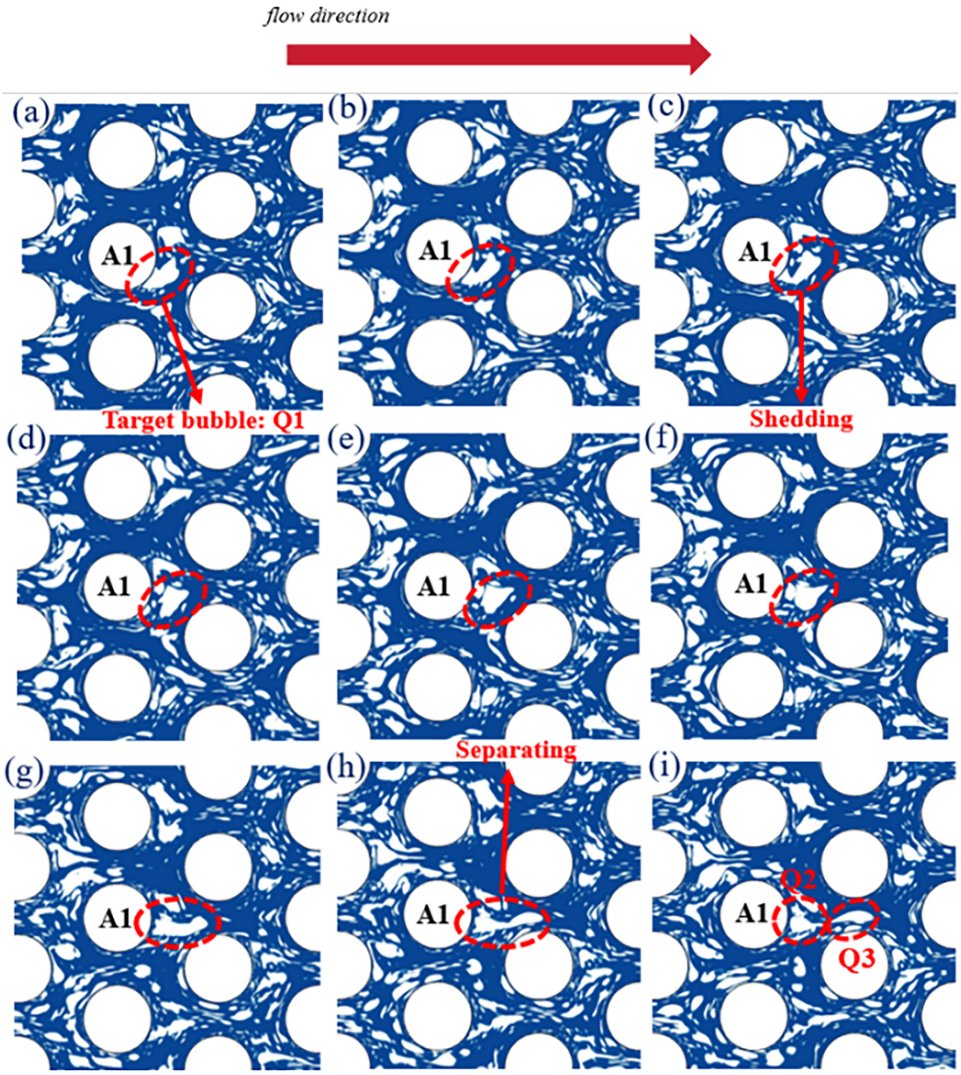


Figure 22: Bubble shedding and separation processes around the tube array: **(a)** t_n; **(b)** t_{n+1}; **(c)** t_{n+2}; **(d)** t_{n+3}; **(e)** t_{n+4}; **(f)** t_{n+5}; **(g)** t_{n+6}; **(h)** t_{n+7}; **(i)** t_{n+8}.

The foregoing analyses of phase distribution, pressure fields, velocity structures and wake evolution yield a consistent physical explanation for the void-fraction-dependent vibration response. The tight correspondence between gas–liquid flow behavior and structural oscillation confirms that the observed vibrations arise from genuine two-phase fluid–structure interactions rather than numerical artifacts. At low void fractions with dispersed bubble flow, the continuous liquid phase dominates cross-flow momentum transfer, sustaining a large cross-tube pressure difference and pronounced drag-direction vibration; discrete small bubbles minimally disrupt coherent wake vortex shedding, leaving the lift response governed by conventional vortex-induced excitation. With increasing void fraction, bubble coalescence drives a transition to slug-like flow with prominent intermittent gas–liquid interfaces: the diminished continuous liquid phase weakens momentum transfer and reduces the time-averaged windward–leeward pressure difference, attenuating drag-direction vibration, while large-scale gas pocket impingement and interface motion introduce intermittent surface pressure fluctuations and modulate wake coherence, accounting for the slight rise in lift-direction RMS amplitude. These results demonstrate that two-phase flow-induced vibration is governed by the coupled

effects of flow pattern evolution, circumferential pressure redistribution and unsteady wake modulation, with directional vibration responses intrinsically linked to local gas–liquid interaction behaviors.

5 Conclusion

In this study, the flow-induced vibration characteristics of cylindrical heat exchange tubes in wind turbine heat exchangers under gas–liquid two-phase flow were investigated using a CFD–CSD coupling approach. Based on the numerical results of the single-tube and tube-array models, the main conclusions are drawn as follows:

(1) Compared with single-phase flow, gas–liquid two-phase flow significantly alters the vibration response of the cylindrical heat exchange tube. For the single-tube configuration, the displacement response becomes more irregular under two-phase conditions, and the vibration in the drag direction is notably enhanced.

(2) For the single-tube model, the vibration response intensifies with increasing inlet velocity. When the inlet velocity rises from 0.1 to 0.6 m/s, the maximum drag-direction displacement under two-phase flow increases from 0.0462 to 0.2788 mm, indicating an elevated flow-induced vibration risk at higher flow velocities.

(3) Frequency-domain results show that the dominant vibration frequency under two-phase flow is mainly concentrated within 56–58 Hz in the drag direction for the single-tube model, and is insensitive to inlet velocity variations. In contrast, the dominant frequency under single-phase flow increases markedly with inlet velocity, indicating that two-phase flow fundamentally changes the flow excitation characteristics of the tube. For the tube-array model, the dominant frequencies lie in the range of 53–56 Hz.

(4) In the tube-array model, the void fraction exerts a significant influence on the vibration response of target tube T1. With increasing void fraction, the drag-direction vibration amplitude (both peak and RMS values) decreases, whereas the lift-direction RMS amplitude exhibits a slight increasing trend. The flow pattern evolves from dispersed bubble flow to slug-like flow as the void fraction increases, which is the essential cause of the directional difference in vibration variation.

(5) Under gas–liquid two-phase cross-flow, the vibration response of the target tube in the tube array is dominated by drag-direction motion. Therefore, drag-direction vibration should be given priority in the structural stability evaluation and vibration control design of heat exchanger tubes in wind turbine cooling systems.

Acknowledgement: The authors would like to thank all those who have contributed to this paper for their valuable assistance.

Funding Statement: This work is supported by Central Government Guided Local Science and Technology Development Fund Projects (2025ZY01009).

Author Contributions: The authors confirm their contributions to the paper as follows: Tianyu Song, Zeshuai Chen and Ruiliang Wang contributed to the conception and design of the study. Tianyu Song, Zeshuai Chen and Qian Chen performed the numerical simulations, data analysis and visualization. Congbo Zheng, Di Tang, Wenxi Shi and Lang Xu provided technical support, resources and guidance for the engineering background of the study. Tianyu Song prepared the original draft. Zeshuai Chen, Ruiliang Wang, Congbo Zheng and Di Tang reviewed and revised the manuscript. Ruiliang Wang supervised the study and was responsible for project administration. All authors reviewed and approved the final version of the manuscript.

Availability of Data and Materials: Not applicable.

Ethics Approval: Not applicable.

Conflicts of Interest: The authors declare no conflicts of interest.

Nomenclature

Symbol	Definition	Unit
C_D	Drag coefficient	–
C_L	Lift coefficient	–
C_P	Pressure coefficient	–
c	Equivalent damping coefficient per unit length	$N{\cdot}s/m^2$
d	Outer diameter of heat exchange tube	mm
F_D	Drag force	N
F_L	Lift force	N
f_n	Structural natural frequency	Hz
g	Gravitational acceleration	m/s^2
h	Longitudinal tube pitch	mm
k	Equivalent stiffness per unit length	N/m^2
l	Transverse tube spacing	mm
m	Equivalent mass per unit length	kg/m
p	Static pressure	Pa
R_e	Reynolds number	–
t	Time	s
V	Inlet velocity	m/s
α	Void fraction (inlet volumetric gas fraction)	–
ζ	Damping ratio	–
μ	Dynamic viscosity	Pa·s
ρ	Density	kg/m^3
σ	Surface tension coefficient	N/m
Subscripts		
g	Gas phase	
l	Liquid phase	
Abbreviations		
CFD	Computational Fluid Dynamics	
CSD	Computational Structural Dynamics	
SST	Shear Stress Transport	
VIV	Vortex-Induced Vibration	
FSI	Fluid–Structure Interaction	
VOF	Volume of Fluid	
RMS	Root Mean Square	
FFT	Fast Fourier Transform	
PSD	Power Spectral Density	

References

1. Ji J, Zhang C, Zhang X, Chen Y. Recent research advances in wind turbine thermal management technologies. Renew Sustain Energy Rev. 2025;208(1):114983. doi:10.1016/j.rser.2024.114983.

2. Taras P, Nilifard R, Zhu ZQ, Azar Z. Cooling techniques in direct-drive generators for wind power application. Energies. 2022;15(16):5986. doi:10.3390/en15165986.
3. Zhu X, Hu X, Zhang L, Li W, Gong L, Yu W, et al. Research and analysis of liquid cooling heat dissipation equipment for insulated-gate bipolar transistor modules of wind power converters based on the finite element analysis method. Machines. 2024;12(10):699. doi:10.3390/machines12100699.
4. Fazylova A, Napadailo Y, Rybina GV, Tultayev B, Iliev T, Stoyanov I. Modeling the thermal state of a wind turbine generator considering external factors. Eng Proc. 2025;104(1):88. doi:10.3390/engproc2025104088.
5. Blevins RD. Flow-induced vibration. 2nd ed. New York, NY, USA: Van Nostrand Reinhold; 1990.
6. Weaver DS, Fitzpatrick JA. A review of cross-flow induced vibrations in heat exchanger tube arrays. J Fluids Struct. 1988;2(1):73–93. doi:10.1016/s0889-9746(88)90137-5.
7. Connors HJ. Fluidelastic vibration of tube arrays excited by cross flow. In: Proceedings of the ASME Winter Annual Meeting, Symposium on Flow Induced Vibration in Heat Exchangers; 1970 Dec 1; New York, NY, USA. p. 42–56.
8. Pettigrew MJ, Taylor CE. Fluidelastic instability of heat exchanger tube bundles: review and design recommendations. J Press Vessel Technol. 1991;113(2):242–56. doi:10.1115/1.2928752.
9. Pettigrew MJ, Taylor CE. Vibration analysis of shell-and-tube heat exchangers: an overview: part 1: flow, damping, fluidelastic instability. J Fluids Struct. 2003;18(5):469–83. doi:10.1016/j.jfluidstructs.2003.08.007.
10. Pettigrew MJ, Taylor CE. Vibration analysis of shell-and-tube heat exchangers: an overview: part 2: vibration response, fretting-wear, guidelines. J Fluids Struct. 2003;18(5):485–500. doi:10.1016/j.jfluidstructs.2003.08.008.
11. Yin Y, Wang Z, Ma M, Zhang J, Xu Y, Li L, et al. Coupling vibration analysis of heat exchanger tube bundles under different stiffness conditions. Sci Rep. 2024;14(1):3953. doi:10.1038/s41598-024-53855-x.
12. Benguigui W, Pinto C, Ries O. Experimental investigation on two-phase cross-flow-induced vibration of a cylinder in a confined channel. J Fluids Struct. 2023;120(5):103909. doi:10.1016/j.jfluidstructs.2023.103909.
13. Spina G, Benguigui W, Brillant G, Vivaldi D, Colin C. Local-scale experimental investigation of a two-phase cross-flow in a tube bundle and flow-induced vibration; Bubbly flow regime. Nucl Eng Des. 2025;433:113836. doi:10.1016/j.nucengdes.2025.113836.
14. Álvarez-Briceño R, Kanizawa FT, Ribatski G, de Oliveira LPR. Experimental estimation of equivalent loads on upward two-phase crossflow in tube bundles via Kalman filtering. J Fluids Struct. 2023;120(10):103900. doi:10.1016/j.jfluidstructs.2023.103900.
15. Lagrange R, Panunzio D, Piteau P, Delaune X, Antunes J. A new criterion for the instability threshold of a square tube bundle subject to an air-water cross-flow. J Fluids Struct. 2023;122:103980. doi:10.1016/j.jfluidstructs.2023.103980.
16. Khan U, Pao W, Sallih N. A review: factors affecting internal two-phase flow-induced vibrations. Appl Sci. 2022;12(17):8406. doi:10.3390/app12178406.
17. Hirt CW, Nichols BD. Volume of fluid (VOF) method for the dynamics of free boundaries. J Comput Phys. 1981;39(1):201–25. doi:10.1016/0021-9991(81)90145-5.
18. Haile SG, Woschke E, Tibba GS, Pandey V. Internal two-phase flow induced vibrations: a review. Cogent Eng. 2022;9(1):2083472. doi:10.1080/23311916.2022.2083472.
19. Turek S, Hron J. Proposal for numerical benchmarking of fluid-structure interaction between an elastic object and laminar incompressible flow. In: Fluid-structure interaction. Berlin/Heidelberg, Germany: Springer; 2007. p. 371–85. doi:10.1007/3-540-34596-5_15.
20. Bamidele OE, Ahmed WH, Hassan M. Two-phase flow induced vibration of piping structure with flow restricting orifices. Int J Multiph Flow. 2019;113(5):59–70. doi:10.1016/j.ijmultiphaseflow.2019.01.002.
21. Tang D, Bao S, Xu M, Luo L, Lv B, Yu L, et al. On the number of tubes required to study oscillating vortices and frequency spectrums of tube arrays in cross flow. Ann Nucl Energy. 2019;124(4):198–210. doi:10.1016/j.anucene.2018.10.008.
22. Li C, Zhao W, Liu H, Xue Y, Yang Y, Chen W. Gas kinetic scheme coupled with high-speed modifications for hypersonic transition flow simulations. Entropy. 2024;26(2):173. doi:10.3390/e26020173.

23. Tang D, Bao S, Luo L, Zhu H, Cui H. A CFD/CSD coupled method with high order and its applications in flow induced vibrations of tube arrays in cross flow. Ann Nucl Energy. 2019;130(5):347–56. doi:10.1016/j.anucene.2019.03.003.
24. Tian Z, Zheng W, Li X, Zheng L, Jiang Y. Numerical investigation on condensation heat transfer performance of mixed hydrocarbon refrigerant in spirally tubes. Int J Refrig. 2022;139(9):13–24. doi:10.1016/j.ijrefrig.2022.04.001.
25. Fu X, Fu S, Han Z, Niu Z, Zhang M, Zhao B. Numerical simulations of 2-DOF *Vortex*-induced vibration of a circular cylinder in two and three dimensions: a comparison study. J Ocean Eng Sci. 2025;10(4):395–410. doi:10.1016/j.joes.2023.08.006.
26. Khalak A, Williamson CHK. Dynamics of a hydroelastic cylinder with very low mass and damping. J Fluids Struct. 1996;10(5):455–72. doi:10.1006/jfls.1996.0031.
27. Wu ZY, Wang H, Cai WH, Jiang YQ. Numerical investigation of boiling heat transfer on the shell-side of spiral wound heat exchanger. Heat Mass Transf. 2016;52(9):1973–82. doi:10.1007/s00231-016-1867-5.
28. Li J, Hu H, Wang H. Numerical investigation on flow pattern transformation and heat transfer characteristics of two-phase flow boiling in the shell side of LNG spiral wound heat exchanger. Int J Therm Sci. 2020;152:106289. doi:10.1016/j.ijthermalsci.2020.106289.
29. Cheng L, Xia G. Flow patterns and flow pattern maps for adiabatic and diabatic gas liquid two phase flow in microchannels: fundamentals, mechanisms and applications. Exp Therm Fluid Sci. 2023;148:110988. doi:10.1016/j.expthermflusci.2023.110988.
30. Zhang J, Lei L, Cheng C, Huang C, Xiao Q, Xin G, et al. Experimental investigations of gas–liquid two-phase flow in a horizontal mini pipe: flow regime, void friction, and frictional pressure drops. Phys Fluids. 2023;35(1):013333. doi:10.1063/5.0135369.
31. Franca FA, Bannwart AC, Camargo RMT, Gonçalves MAL. Mechanistic modeling of the convective heat transfer coefficient in gas-liquid intermittent flows. Heat Transf Eng. 2008;29(12):984–98. doi:10.1080/01457630802241091.